A Weighted Bounded Hessian Variational Model for Image Labeling and Segmentation

Yijie Yang[†], Qiuxiang Zhong[†], Yuping Duan[∗] and Tieyong Zeng[§]

[†]*The first two authors are equally contributed. Center for Applied Mathematics, Tianjin University, China, Tianjin, 300072, China,*
`E-mail: {yangyijie,zhongqiuxiang}@tju.edu.cn`

[∗]*Corresponding author. Center for Applied Mathematics, Tianjin University, 300072, China,* `E-mail: yuping.duan@tju.edu.cn`

[§]*Department of mathematics, The Chinese University of Hong Kong, Shatin, NT, Hong Kong,* `E-mail: zeng@math.cuhk.edu.hk`

Abstract

Natural images are usually composed of multiple objects at different scales in flat and slanted regions. Traditional labeling/segmentation approaches based on total variation minimization may produce staircase results with discontinuities and rough boundaries. In this paper, we propose a novel weighted variational model for image labeling/segmentation in the space of functions of bounded Hessian, the weights of which are automatically estimated based on edge information of the observed images. Especially, by minimizing the combined first and second-order regularizer, our model can overcome the shortage of total variation and provide more meaningful results. The efficient alternating direction method of multipliers based algorithm is established, all subproblems of which can be solved by either the fast Fourier transform or closed-form solution. We further introduce the weighted bounded Hessian regularizer into the two-stage segmentation framework for dealing with noisy and blurry image segmentation problems. Numerous experiments are conducted on both two-phase and multi-phase labeling/segmentation problems. By comparing with several state-of-the-art methods both qualitatively and quantitatively, it demonstrates that the proposed models can prominently improve the accuracy of image labeling and segmentation.

Keywords: Image labeling, segmentation, bounded Hessian, spatially adaptive weights, ADMM

---

1. Introduction

Image labeling and segmentation are fundamental tasks in image processing and computer vision, which aim to find a partition of an image domain into disjoint regions (phases or classes) according to some optimization rules. Various variational and Partial Differential Equations (PDEs)-based methods have been proposed for image labeling and segmentation problems.

Mumford and Shah [1] proposed an energy minimization problem which approximates the true solution by finding optimal piecewise smooth approximations. Let $\Omega \subset \mathbb{R}^2$ be a bounded open connected set, Γ be a compact curve in Ω and $I : \Omega \to \mathbb{R}$ be a given image. The Mumford-Shah (MS) model can be formulated as the minimization of the following energy functional

$$\min_{u,\Gamma} \frac{\lambda}{2} \int_{\Omega} (I-u)^2 dx + \beta \int_{\Omega \backslash \Gamma} |\nabla u|^2 dx + |\Gamma|, \tag{1}$$

where λ, β are positive parameters and $u : \Omega \to \mathbb{R}$ is continuous or even differentiable in $\Omega \backslash \Gamma$ but may be discontinuous across Γ. Since the Mumford-Shah functional is non-convex and the integral regions of the last two terms are discontinuous, it is very challenging to find its minimizer.

Chan and Vese introduced the method of active contour without edges (ACWE) by restricting $\nabla u \equiv 0$ on $\Omega \backslash \Gamma$ for two-phase and multi-phase segmentation problems in [2, 3], respectively. The ACWE model used the piecewise constant solutions to approximate the Mumford-Shah model such as

$$\min_{c_1,c_2,\Gamma} \frac{\lambda}{2} \Big(\int_{\Sigma} (I-c_1)^2 dx + \int_{\Omega \backslash \Sigma} (I-c_2)^2 dx \Big) + |\Gamma|, \tag{2}$$

where $c_1, c_2 \in \mathbb{R}$ are the average values of the pixels inside and outside Γ for the two-phase segmentation. When the intensity values redc_1, c_2 are known in advance, the ACWE model turns to be the continuous Potts model, which has intensively studied for image labeling problems. However, the minimization of both the ACWE model and Potts model are still non-convex due to the non-convex binary constraint of the labeling function, which may be stuck into the local minimum and are sensitive to the initializations.

Chan, Esedoglu and Nikolova [4] reformulated the ACWE model into a convex minimization by relaxing the binary constraint into a convex one. The authors proved that thresholding the solution of the relaxed convex problem by any value in [0,1] can yield a globally optimal labeling solution. Since then, fast and reliable convex optimization-based algorithms have been developed and applied to image labeling and segmentation problems [5, 6, 7]. Bresson *et al.* [8] pursued a global minimizer of active contour model (GMAC), which minimized the following energy functional for image labeling

$$\min_{u \in [0,1]} \lambda \int_{\Omega} (f_1^2 - f_2^2) u dx + \int_{\Omega} g(x) |\nabla u| dx, \tag{3}$$

where $g : \Omega \to \mathbb{R}^+$ contains boundary information of objects. The usual choice of g is an edge indicator function vanishing at object boundaries such as $g(I) = \frac{1}{1+\gamma|\nabla I|^2}$ with γ being a positive parameter, which can precisely identify the boundaries of the objects. Lellmann *et al.* [9] applied the Douglas-Rachford splitting to the convex formulation of the Potts model for multi-class image labeling problems. Pock *et al.* [10] proposed a convex relaxation approach for computing the minimal partitions based on Potts model, which was solved by the primal-dual algorithm. The Chambolle dual algorithms have been proposed to solve the Potts model for the continuous multi-partitioning problem in [11, 12]. Yuan *et al.* [13, 14] developed the continuous max-flow model for the two-phase and multi-phase labeling problems, which gives another dual formulation of the Potts model.

In general, noise and blur may be contained in the observed images. Therefore, it is reasonable to restore the clean image and then perform the segmentation based on the restoration image. Cai, Chan and Zeng [15] proposed a two-stage segmentation method, which is a convex variant of the Mumford-Shah model. In the first stage, a smooth solution u is estimated from the given image I by minimizing the following functional

$$\min_{u} \frac{\lambda}{2}\int_{\Omega}(I-Ku)^2dx+\beta\int_{\Omega}|\nabla u|^2dx+\int_{\Omega}|\nabla u|dx, \tag{4}$$

where K can be the identify operator or a blurring operator. In the second stage, a thresholding step is applied to realize the segmentation. Since then, the two-stage framework has been widely used for image labeling/segmentation. Chan, Yang and Zeng [16] used the two-stage method for segmenting blurry images in the presence of Poisson or multiplicative Gamma noise. Duan *et al.* [17] proposed a ℓ_0 regularized Mumford-Shah model based on the two-stage segmentation framework, which was further modified using the high-order regularizer for medical image segmentation in [18]. Duan *et al.* [19] solved the Euler's elastica regularized Mumford-Shah model in a two-stage segmentation framework. Liu *et al.* [20] presented a two-stage weighted variational model for selective image segmentation. Chen, Li and Zeng [21] used the two-stage segmentation method to solve the Rician noise corrupted images. Cai *et al.* [22] restudied the linkage between the piecewise constant Mumford-Shah model and ROF model, and proposed the thresholded-ROF model to illustrate the virtue of managing image segmentation through image restoration techniques.

Due to the great success of the deep learning approaches in digit recognition, categorizing and detecting objects in images, the convolutional neural networks (CNNs) have also been applied to pixel-wise labeling and segmentation [23, 24, 25, 26]. Although CNNs have shown their advantages in the semantic segmentation tasks, it is still difficult for a CNN model to discriminate pixels belonging to similar receptive fields around the object boundaries. Therefore, traditional techniques have been further introduced into deep networks to produce uniform segmentation results. For example, Hu *et al.* [27] proposed a deep level set network to drive the network to learn a level set function for salient objects, which can output more accurate boundaries and compact saliency maps. Duan *et al.* [28] used a fully convolutional network to learn the probability maps, which were incorporated in a single nested level set optimization framework for multi-region segmentation with high efficiency. Besides, the annotated training set may not be large enough to contain all shapes and apparent variations of the target objects, for which the level set-based methods can be used to regularize the results of deep networks to produce good generalization [29].

1.1. Motivation and our contributions

The main drawback of the aforementioned total variation-based labeling/segmentation methods is their limitation in processing natural images, which contain not only flat regions and jumps, but also some slanted regions. The total variation minimization will introduce the so-called staircase effect in the piecewise smooth regions and result in the discontinuous segmentation results. High-order regularities can be used to overcome the shortage of TV term. The bounded Hessian regularizer was first proposed by Chambolle and Lions in [30] by means of an inf-convolution of two convex regularizers. Le and Vese [31] introduced the inf-convolution for piecewise smooth segmentation problem by decomposing $u = v + w$ and minimizing

$$\min_{v,w} \lambda \int_{\Omega} \left((f_1 - w)^2 - (f_2 - w)^2\right) v dx + \beta_1 \int_{\Omega} |\nabla w| dx + \beta_2 \int_{\Omega} |\nabla^2 w| dx + \int_{\Omega} |\nabla v| dx, \tag{5}$$

where $\nabla^2 w$ denotes the Hessian operator of w over image domain Ω, i.e.,

$$\nabla^2 w = \begin{pmatrix} \frac{\partial^2 w}{\partial x^2} & \frac{\partial^2 w}{\partial x \partial y} \\ \frac{\partial^2 w}{\partial y \partial x} & \frac{\partial^2 w}{\partial y^2} \end{pmatrix},$$

and v is a piecewise constant component to capture edges and discontinuities, w is a smooth component to capture global inhomogeneity. Note that the infimal convolution of the image function $u = v + w$ with $v \in \mathrm{BV}(\Omega)$ and $w \in \mathrm{BH}(\Omega)$, still gives a function u such that $u \in \mathrm{BV}(\Omega)$. In order to obtain a more regular solution, Papafitsoros and Schönlieb [32] considered the combined first and second-order variational approach for image restoration

$$\min_{u} \frac{1}{2} \int_{\Omega} (I - u)^2 dx + \alpha \int_{\Omega} |\nabla u| dx + \beta \int_{\Omega} |\nabla^2 u| dx, \tag{6}$$

the minimizer of which is in $\mathrm{BH}(\Omega)$ as a whole. The simple and convex high-order extension of total variation regularizer can provide faithful restoration result with good continuation by reducing the staircase effect. Such combined first and second-order regularizer has been further studied for image inpainting [33] and speckle noise removal [34], both of which achieved state-of-the-art performance.

In this paper, **our first contribution** is to propose a weighted bounded Hessian variational model for image labeling and segmentation. Unlike existing high-order regularization segmentation models such as Euler's elastica [35] and mean curvature [36], which are nonconvex, nonsmooth and nonlinear, the proposed model is coercive, lower semi-continuous and convex with the theoretical guarantee of the existence of a solution. Thus, numerous fast algorithms for convex minimization can be used to solve the proposed model. We develop an efficient alternating direction method of multipliers (ADMM) based algorithm and discuss the convergence under certain conditions.

Another important contribution of our work is that we investigate an automatic method to estimate the weight functions for the first and second-order regularizer accordingly. Observed from the Mumford-Shah model, the smooth regularizer should be applied to homogeneous areas, while the piecewise constant regularizer should be acted on the edge sets. Therefore, we use the edge detector function and the total variation of the edge detector function as the weight functions for the smooth regularizer and piecewise constant regularizer, respectively. Numerical results demonstrate that the proposed model outperforms state-of-the-art variational models

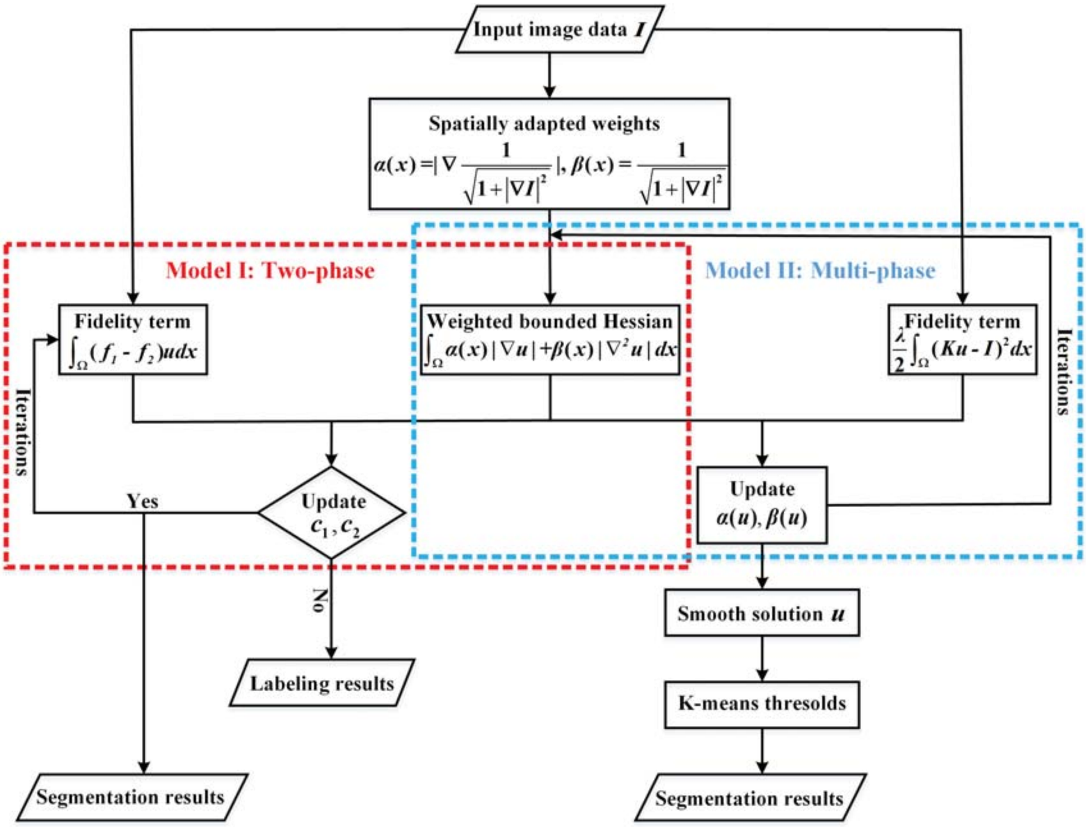

Figure 1: Overall flowchart of the proposed models, where the weighted bounded Hessian regularization is used for two-phase and multi-phase segmentation.

on various image labeling/segmentation problems, which can smooth out unimportant details in homogeneous regions and preserve characteristic structures such as edges, sharp corners, etc. In the end, we extend the weighted bounded Hessian variational model for multi-phase segmentation in a two-stage framework for noisy and blurry image segmentation. The processing flow is outlined in Figure 1, where two models are considered in our work.

The rest of the paper is organized as follows. In Section 2, we propose the hybrid weighted bounded Hessian variational model and establish the existence of a solution. Section 3 presents the ADMM-based numerical algorithm and provides the convergence analysis for the ADMM algorithm under certain conditions. The implementation details and evaluation criteria are discussed in Section 4 and the comprehensive numerical results are conducted on image labeling and segmentation problems in Section 5. Section 6 attempts to evaluate the performance of weighted bounded Hessian variational model in the two-stage segmentation framework with numerical tests. Finally, conclusion and future work are discussed in Section 7.

2. Weighted Bounded Hessian Variational Model

2.1. Preliminaries and notations

Letting $X \subset \mathbb{R}^n$ be a measurable space and $f : X \to \mathbb{R}$ be a measurable function, we define

$$L^p(X) = \{f \mid \|f\|_p < \infty,\ 1 \le p \le \infty\},$$

where $\|f\|_p = (\int_X |f|^p dx)^{\frac{1}{p}}$ with $1 \le p < \infty$, and $\|f\|_\infty = \sup_{x\in X} |f(x)|$. If $p = 2$, we denote $\|f\| := \|f\|_2$. The inner product of two functions f and g is given by $\langle f, g\rangle = \int_X f(x)g(x)dx$.

We further define the Sobolev space on Ω as

$$W^{1,p}(\Omega) = \big\{u \in L^p(\Omega) : \nabla u \in L^p(\Omega)\big\},$$

where ∇u is the weak gradient of u. More precisely, we define

$$\|\nabla u\|_1 := \int_\Omega |\nabla u| dx = \sup\left\{ \int_\Omega u \operatorname{div}\phi dx; \phi \in \mathscr{C}_0^\infty(\Omega, \mathbb{R}^n), \|\phi\|_\infty \le 1\right\},$$

where $\operatorname{div}\phi = \sum_{i=1}^n \frac{\partial \phi_i}{\partial x_i}(x)$, $\mathscr{C}_0^\infty(\Omega, \mathbb{R}^n)$ is the space of continuous differentiable functions with compact support in Ω, and $\|\phi\|_\infty = \sup_x \sqrt{\sum_i \phi_i^2(x)}$. The space of functions of bounded variation is denoted by $\mathrm{BV}(\Omega)$, which is a Banach space equipped with the norm $\|u\|_{\mathrm{BV}(\Omega)} = \|u\|_1 + \|\nabla u\|_1$. We refer the readers to [37] for more detailed introduction of BV space.

Following [32] and [38], we introduce the space of functions of bounded Hessian $\mathrm{BH}(\Omega)$ (also denoted as $\mathrm{BV}^2(\Omega)$). It consists of all functions $u \in W^{1,1}(\Omega)$ whose distributional Hessian can be represented by an $\mathbb{R}^n \times \mathbb{R}^n$-valued finite Radon measure, i.e.,

$$\mathrm{BH}(\Omega) = \big\{u \in W^{1,1}(\Omega) : \|\nabla^2 u\|_1 < \infty\big\},$$

with

$$\|\nabla^2 u\|_1 := \int_\Omega |\nabla^2 u| dx = \sup\left\{ \int_\Omega u \operatorname{div}^2\phi dx; \phi \in \mathscr{C}_0^\infty(\Omega, \mathbb{R}^{n\times n}), \|\phi\|_\infty \le 1\right\}.$$

Therefore, it is immediate that $W^{2,1}(\Omega) \subset \mathrm{BH}(\Omega)$ and $\mathrm{BH}(\Omega)$ is a Banach space equipped with norm $\|u\|_{\mathrm{BH}(\Omega)} = \|u\|_1 + \|\nabla u\|_1 + \|\nabla^2 u\|_1$. In the following, we summarize the main properties of $\mathrm{BH}(\Omega)$ with more details in [32].

- (Embedding) If Ω has a Lipschitz boundary and it is connected, it can be shown that there exist positive constants C_1 and C_2 such that

  $$\int_\Omega |\nabla u| dx \le C_1 \int_\Omega |\nabla^2 u| dx + C_2 \int_\Omega |u| dx, \quad \forall u \in \mathrm{BH}(\Omega),$$

  and $\mathrm{BH}(\Omega)$ is continuously embedded in $L^2(\Omega)$ when $n = 2$.

- (Weak* Convergence in $\mathrm{BH}(\Omega)$) Let $\{u_k\}_{k\in\mathbb{N}}$ and u belong to $\mathrm{BH}(\Omega)$. We say $\{u_k\}_{k\in\mathbb{N}}$ converges to u weakly* in $\mathrm{BH}(\Omega)$ if

  $$\|u_k - u\|_1 \to 0, \quad \|\nabla u_k - \nabla u\|_1 \to 0,$$

  and

  $$\int_\Omega u_k \mathrm{div}^2 \phi dx \to \int_\Omega u \mathrm{div}^2 \phi dx, \ \forall \phi \in \mathscr{C}_0^\infty(\Omega, \mathbb{R}^{n\times n}).$$

- (Compactness in $\mathrm{BH}(\Omega)$) Suppose that the sequence $\{u_k\}_{k\in\mathbb{N}}$ is bounded in $\mathrm{BH}(\Omega)$. Then there exists a subsequence $\{u_{k_\ell}\}_{\ell\in\mathbb{N}}$ and a function $u \in \mathrm{BH}(\Omega)$ such that $\{u_{k_\ell}\}_{\ell\in\mathbb{N}}$ converges to u weakly* in $\mathrm{BH}(\Omega)$.

- (Lower semi-continuity) The semi-norm $\|\nabla^2 u\|_1$ is lower semi-continuous endowed with strong topology of $W^{1,1}(\Omega)$. More precisely, if $\|u_k - u\|_1 \to 0$, $\|\nabla u_k - \nabla u\|_1 \to 0$, then

  $$\int_\Omega |\nabla^2 u| dx \le \liminf_{k\to\infty} \int_\Omega |\nabla^2 u_k| dx.$$

  In particular, for $\{u_k\}_{k\in\mathbb{N}} \in W^{1,1}(\Omega)$, if $\liminf\limits_{k\to\infty} \int_\Omega |\nabla^2 u_k| dx < \infty$, there is $u \in \mathrm{BH}(\Omega)$.

2.2. *Weighted bounded Hessian variational model*

Considering the limitation of the TV regularizer in dealing with smooth image labeling, we introduce the bounded Hessian variational model by minimizing the following energy functional

$$E(u) := \int_\Omega \alpha(x)|\nabla u| dx + \int_\Omega \beta(x)|\nabla^2 u| dx + \lambda \int_\Omega (f_1 - f_2) u dx, \tag{7}$$

subject to the box constraint $u \in [0,1]$. Because the images are comprised of multiple objects at different scales, it is more reasonable to choose α and β as spatially adaptive values rather than constants. Therefore, we define $\alpha(x), \beta(x) : \Omega \to \mathbb{R}$ to be the spatial varying weight functions for the first and second-order regularizer, respectively, both of which can be estimated in advance according to certain rules and will be discussed later.

It is easy to check that the functional $E(u)$ in (7) is in $W^{2,1}(\Omega)$. By extending the functional into a larger Banach space $\mathrm{BH}(\Omega)$ and using the properties of $\mathrm{BH}(\Omega)$, we can establish the existence of a solution for minimizing the energy functional (7) as follows.

Theorem 2.1. *If $\alpha(x), \beta(x) \in C(\bar{\Omega})$ and $\alpha(x) > 0$, $\beta(x) > 0$ for all $x \in \bar{\Omega}$. Then, for a fixed $\lambda > 0$, the spatially adaptive bounded Hessian variational model* (7) *is convex and there exists a minimizer u^* in* $\mathrm{BH}(\Omega)$.

Proof. *Let $\{u_k\}_{k\in\mathbb{N}}$ in* $\mathrm{BH}(\Omega)$ *be a minimizing sequence of* (7)*, and let $M > 0$ be an upper bound for $E(u_k)_{k\in\mathbb{N}}$ such that*

$$\int_\Omega \alpha(x)|\nabla u_k| dx \le M, \ \int_\Omega \beta(x)|\nabla^2 u_k| dx \le M, \text{ and } \lambda \int_\Omega (f_1 - f_2) u_k dx \le M. \tag{8}$$

By the conditions $\alpha(x) > 0$ *and* $\beta(x) > 0$ *for all* $x \in \bar{\Omega}$*, we have the boundness of* $\alpha(x)$ *and* $\beta(x)$*. We suppose*

$$\alpha_0 \leq \alpha(x) \leq \alpha_1 \text{ and } \beta_0 \leq \beta(x) \leq \beta_1, \ \forall x \in \bar{\Omega}, \tag{9}$$

where α_0*,* α_1*,* β_0 *and* β_1 *are some positive constants.*

According to (8) *and* (9)*, it follows that*

$$\int_\Omega |\nabla u_k| dx \leq \frac{M}{\alpha_0} \text{ and } \int_\Omega |\nabla^2 u_k| dx \leq \frac{M}{\beta_0}.$$

Moreover, on account of (8) *with the fixed parameters* c_1 *and* c_2*, it can be obtained that*

$$\int_\Omega (f_1 - f_2) u_k dx \leq \frac{M}{\lambda},$$

that is

$$\int_\Omega u_k dx \leq \frac{M}{\lambda \|f_1 - f_2\|}.$$

Therefore, the sequence $\{u_k\}_{k\in\mathbb{N}}$ *is uniformly bounded in* $L^1(\Omega)$*.*

Based on the Minkowski's inequality and the boundedness of sequence $\{u_k\}_{k\in\mathbb{N}}$*, there exists a constant* C *such that*

$$\|u_k\|_{\mathrm{BH}(\Omega)} = \|u_k\|_1 + \|\nabla u_k\|_1 + \|\nabla^2 u_k\|_1 \leq C, \ \forall k \in \mathbb{N}. \tag{10}$$

Hence, according to the compactness theorem, there is a subsequence in $\{u_k\}_{k\in\mathbb{N}}$*, denoted* $\{u_{k_\ell}\}_{\ell\in\mathbb{N}}$*, such that converges to* u^* *weakly** *in* $\mathrm{BH}(\Omega)$*. By the lower semi-continuity of* $E(u)$ *and Fatou's lemma, we have*

$$\int_\Omega (f_1 - f_2) u^* dx \leq \liminf_{\ell\to\infty} \int_\Omega (f_1 - f_2) u_{k_\ell} dx,$$

$$\int_\Omega |\nabla u^*| dx \leq \liminf_{\ell\to\infty} \int_\Omega |\nabla u_{k_\ell}| dx,$$

$$\int_\Omega |\nabla^2 u^*| dx \leq \liminf_{\ell\to\infty} \int_\Omega |\nabla^2 u_{k_\ell}| dx.$$

It follows that

$$E(u^*) \leq \liminf_{\ell\to\infty} E(u_{k_\ell}), \tag{11}$$

i.e., u^* *is a minimizer of* (7)*.*

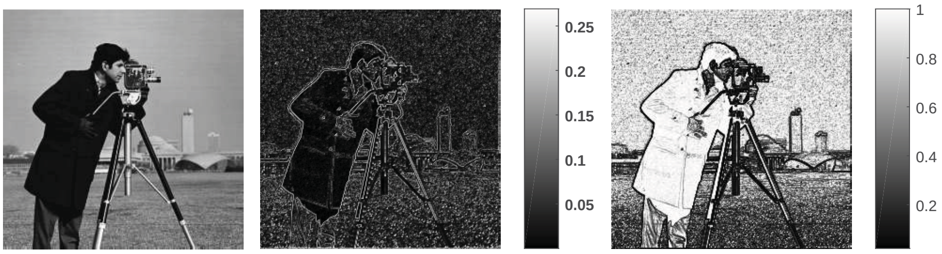

(a) Input image (b) $\alpha(I)$ (c) $\beta(I)$

Figure 2: Spatially adaptive weights $\alpha(I)$ and $\beta(I)$ of the image 'Cameraman' in the proposed model (7), where the step size of finite difference is $h = 5$.

2.3. Automatic estimation of the hybrid weights

The spatially adaptive weights have been discussed for the first and second-order regularizer separately in the literature. As mentioned, the GMAC model (3) used the edge detection function as the weight for total variation. Duan *et al.* [39] introduced the edge diffusivity function as the weight function for the second-order regularization term. To the best of our knowledge, there is no such study on the combined first and second-order regularizer considered in this work. We define the hybrid weights for the proposed model such that $\alpha(x)$ and $\beta(x)$ are functions of the given image I to fully capture the edge information

$$\alpha(I) = \left|\nabla \frac{1}{\sqrt{1+|\nabla I|^2}}\right| \text{ and } \beta(I) = \frac{1}{\sqrt{1+|\nabla I|^2}}. \tag{12}$$

On one hand, the function $\beta(I)$ is the edge indicator function acting as the weight for the smooth regularizer, whereas $\beta(I)$ is large in homogenous regions to smooth out some unnecessary details and textures, and small cross edges to sharpen image edges. On the other hand, the function $\alpha(I)$ is the variation of the edge detector function used as the weight for the first order regularizer such that $\alpha(I)$ is large in edge regions to enhance the first order regularizer for preserving the main edges. In this way, the values of $\alpha(I)$ and $\beta(I)$ ideally coincide with the requirements of the regularization terms for labeling and segmentation tasks. Figure 2 gives an example of $\alpha(I)$ and $\beta(I)$ obtained on the image 'Cameraman', which illustrates $\beta(I)$ automatically stops at the edges and $\alpha(I)$ promotes at the edges as we expected.

3. Numerical Algorithm

3.1. Constrained optimization and ADMM

The alternating direction method of multipliers (ADMM) [40, 41] is applied to solve the proposed spatially adaptive minimization model (7). The ADMM has received great success in solving image processing models such as the classical Rudin-Osher-Fatemi (ROF) model and some high-order variational models, which involve either non-differentiable or higher-order terms.

At the first place, we introduce three auxiliary variables v, w and z to rewrite the original minimization problem into a constrained one such as

$$\begin{aligned} &\min_{u,v,w,z} \int_\Omega \alpha(I)|w|dx + \int_\Omega \beta(I)|z|dx + \lambda \int_\Omega (f_1 - f_2)vdx \\ &\text{s.t. } w = \nabla u,\ z = \nabla^2 u,\ v = u,\ u \in [0,1]. \end{aligned} \tag{13}$$

Based on the well-known augmented Lagrangian method, we can reformulate (13) into the following Lagrangian functional

$$\begin{aligned} \mathscr{L}(u,v,w,z;\lambda_1,\lambda_2,\lambda_3) &= \int_\Omega \alpha(I)|w|dx + \int_\Omega \beta(I)|z|dx + \lambda \int_\Omega (f_1 - f_2)vdx \qquad (14) \\ &+ \frac{r_1}{2}\int_\Omega \big(w - \nabla u + \frac{\lambda_1}{r_1}\big)^2 dx + \frac{r_2}{2}\int_\Omega \big(z - \nabla^2 u + \frac{\lambda_2}{r_2}\big)^2 dx + \frac{r_3}{2}\int_\Omega \big(v - u + \frac{\lambda_3}{r_3}\big)^2 dx + \delta_{\mathscr{D}}(v), \end{aligned}$$

where $\mathscr{D} = [0,1]$, and $\delta_{\mathscr{D}}(v)$ is the characteristic function defined on the set $\mathscr{D}$

$$\delta_{\mathscr{D}}(v) = \begin{cases} 0, & \text{if } v \in \mathscr{D}; \\ +\infty, & \text{otherwise.} \end{cases}$$

In (14), λ_1, λ_2 and λ_3 represent the Lagrange multipliers, and r_1, r_2 and r_3 denote the positive penalty parameters acting as the weights of the penalty terms. In each iteration, we tend to sequentially minimize over the variables u, v, w, z by keeping the reminder variables fixed, and then update the Lagrange multipliers $\lambda_1, \lambda_2, \lambda_3$ using the gradient ascent. The procedure will be repeated until convergence, which means a saddle-point of the augmented Lagrangian functional is obtained.

3.2. Numerical solution to the sub-minimization problems

Given the fixed variables v^k, w^k, z^k and λ_1^k, λ_2^k, λ_3^k, we discuss the solutions to the sub-minimization problems with respect to the variable u, v, w, z in the $(k+1)$-th iteration.

3.2.1. The u-subproblem

The sub-minimization problem with respect to u is formulated as follows

$$\min_u \frac{r_1}{2}\int_\Omega \Big(\nabla u - w^k - \frac{\lambda_1^k}{r_1}\Big)^2 dx + \frac{r_2}{2}\int_\Omega \Big(\nabla^2 u - z^k - \frac{\lambda_2^k}{r_2}\Big)^2 dx + \frac{r_3}{2}\int_\Omega \Big(u - v^k - \frac{\lambda_3^k}{r_3}\Big)^2 dx, \tag{15}$$

the Euler-Lagrange equation of which gives us the following linear PDE

$$(-r_1 \nabla \cdot \nabla + r_2 \nabla^2 \cdot \nabla^2 + r_3)u = -\nabla \cdot (r_1 w^k + \lambda_1^k) + \nabla^2 \cdot (r_2 z^k + \lambda_2^k) + r_3 v^k + \lambda_3^k.$$

Therefore, we can apply the fast Fourier transform (FFT) to solve the above equation, which gives

$$u^{k+1} = \mathscr{F}^{-1}\left(\frac{\mathscr{F}(-\nabla \cdot (r_1 w^k + \lambda_1^k) + \nabla^2 \cdot (r_2 z^k + \lambda_2^k) + r_3 v^k + \lambda_3^k)}{r_3 \mathscr{I} - r_1 \mathscr{F}(\nabla \cdot \nabla)\mathscr{F}^{-1} + r_2 \mathscr{F}(\nabla^2 \cdot \nabla^2)\mathscr{F}^{-1}}\right) \tag{16}$$

with $\mathscr{I}$ being the identity operator, $\mathscr{F}$ and $\mathscr{F}^{-1}$ representing the commonly-used forward and inverse FFT operation, respectively.

3.2.2. The v-subproblem

The sub-minimization problem associated with the variable v can be described as follows

$$\min_{0\le v\le 1} \frac{r_3}{2}\int_\Omega \left(v-u^{k+1}+\frac{\lambda_3^k}{r_3}\right)^2 dx+\lambda\int_\Omega (f_1-f_2)v dx+\delta_{\mathscr{D}}(v), \tag{17}$$

the first-order optimality condition of which is

$$r_3\left(v^{k+1}-u^{k+1}+\frac{\lambda_3^k}{r_3}\right)+\lambda\left(f_1-f_2\right)=0$$

subject to the box constraint $v\in[0,1]$. Thus, we have

$$v^{k+1}=u^{k+1}-\frac{\lambda_3^k}{r_3}-\frac{\lambda(f_1-f_2)}{r_3}.$$

In the subsequent step, we perform a one-step projection of v^{k+1} to take the constraint $0\le v\le 1$ into account such that

$$v^{k+1}=\min\left(\max\left(u^{k+1}-\frac{\lambda_3^k}{r_3}-\frac{\lambda(f_1-f_2)}{r_3},0\right),1\right). \tag{18}$$

3.2.3. The (w,z)-subproblems

The sub-minimization problem of w is a typical L^1 minimization problem with a spatial varying parameter, i.e.,

$$\min_w \int_\Omega \alpha(I)|w|dx+\frac{r_1}{2}\int_\Omega \left(w-\nabla u^{k+1}+\frac{\lambda_1^k}{r_1}\right)^2 dx. \tag{19}$$

Similarly, the sub-minimization problem of the variable z gives

$$\min_z \int_\Omega \beta(I)|z|dx+\frac{r_2}{2}\int_\Omega \left(z-\nabla^2 u^{k+1}+\frac{\lambda_2^k}{r_2}\right)^2 dx. \tag{20}$$

Both w and z can be easily computed based on the closed-form solution such as

$$w^{k+1}=\text{shrinkage}\left(\frac{r_1\nabla u^{k+1}-\lambda_1^k}{r_1},\frac{\alpha(I)}{r_1}\right), \tag{21}$$

and

$$z^{k+1}=\text{shrinkage}\left(\frac{r_2\nabla^2 u^{k+1}-\lambda_2^k}{r_2},\frac{\beta(I)}{r_2}\right), \tag{22}$$

where the shrinkage operator is defined as

$$\text{shrinkage}(a,b)=\max\{|a|-b,0\}\circ\frac{a}{|a|}$$

with $\circ$ denoting the point-wise multiplication.

3.2.4. Lagrange multipliers $(\lambda_1, \lambda_2, \lambda_3)$

In the end, we update the Lagrange multipliers $(\lambda_1, \lambda_2, \lambda_3)$ by gradient ascent as follows

$$\begin{cases} \lambda_1^{k+1} = \lambda_1^k + r_1(w^{k+1} - \nabla u^{k+1}), \\ \lambda_2^{k+1} = \lambda_2^k + r_2(z^{k+1} - \nabla^2 u^{k+1}), \\ \lambda_3^{k+1} = \lambda_3^k + r_3(v^{k+1} - u^{k+1}). \end{cases} \tag{23}$$

To sum up, the efficient ADMM-based algorithm is proposed to deal with the weighted bounded Hessian variational model (7); see Algorithm 1.

Algorithm 1 The ADMM-based algorithm for the weighted bounded Hessian model

```
Input: Input image $I$, regularization parameter $\lambda$, positive constants $c_1, c_2$, penalty parameters $r_1, r_2, r_3$, maximum iteration $K_{\max}$, and stopping threshold $\varepsilon$;
Initialize: $u^0 = v^0 = w^0 = z^0 = \lambda_1^0 = \lambda_2^0 = \lambda_3^0 = 0$, set $k = 0$;
while (not converged and $k \le K_{\max}$) do
  Compute $u^{k+1}$ with fixed $v^k$, $w^k$, $z^k$, $\lambda_1^k$, $\lambda_2^k$ and $\lambda_3^k$ according to (16);
  Compute $v^{k+1}$ with fixed $u^{k+1}$ and $\lambda_3^k$ according to (18);
  Compute $w^{k+1}$ with fixed $u^{k+1}$ and $\lambda_1^k$ according to (21);
  Compute $z^{k+1}$ with fixed $u^{k+1}$ and $\lambda_2^k$ according to (22);
  Update $\lambda_1^{k+1}$, $\lambda_2^{k+1}$ and $\lambda_3^{k+1}$ according to (23);
  Check the convergence condition: $\|u^{k+1} - u^k\|_1 \le \varepsilon \|u^k\|_1$;
end while
```

3.3. Convergence analysis

The convergence of the ADMM-based algorithm for solving the convex composite problems has been studied in [42, 43]. Here, we discuss the convergence of Algorithm 1 for image labeling problems.

Theorem 3.1. *Suppose* $u^{k+1} - u^k \to 0$, $\lambda_1^{k+1} - \lambda_1^k \to 0$, $\lambda_2^{k+1} - \lambda_2^k \to 0$ *and* $\lambda_3^{k+1} - \lambda_3^k \to 0$ *as* $k \to \infty$ *in ADMM-based Algorithm 1. Then the generated sequence* $\{(u^k, v^k, w^k, z^k; \lambda_1^k, \lambda_2^k, \lambda_3^k)\}_{k \in \mathbb{N}}$ *converges to a limit point* $\{(u^*, v^*, w^*, z^*; \lambda_1^*, \lambda_2^*, \lambda_3^*)\}$ *that satisfies the first-order optimality conditions, i.e.,*

$$\begin{cases} \nabla \cdot \lambda_1^* - \nabla^2 \cdot \lambda_2^* - \lambda_3^* = 0, \\ \lambda_3^* + \lambda(f_1 - f_2) = 0, \\ \alpha(I)s^* + \lambda_1^* = 0, \ s^* \in \partial |w^*|, \\ \beta(I)p^* + \lambda_2^* = 0, \ p^* \in \partial |z^*|, \\ w^* = \nabla u^*, \ z^* = \nabla^2 u^*, \ v^* = u^*. \end{cases}$$

Proof. *The proof is sketched in the appendix.*

4. Implementation and Evaluation

In this section, we present the numerical experiments of the proposed spatially adaptive variational model (7) on various image labeling and segmentation applications. To demonstrate the effectiveness and superiority of our proposal, we compare it with several advanced methods on both synthetic and real images. To set up the experimental comparison as fair as possible, the parameters of the comparative methods are selected as suggested in the corresponding papers. All numerical experiments are performed in a Matlab R2016a environment on a desktop with 3.20GHz Intel(R) Core(TM) i7-8700 CPU and 16GB RAM.

In the experiments, we monitor the relative residuals in order to check whether our algorithm converges to a saddle point, which are defined as

$$(R_1^k, R_2^k, R_3^k) = \frac{1}{|\Omega|}(\|w^k - \nabla u^k\|_1, \|z^k - \nabla^2 u^k\|_1, \|v^k - u^k\|_1) \tag{24}$$

with $\|\cdot\|_1$ denoting the L^1 norm on Ω and $|\Omega|$ being the area of image domain. To check the convergence of the iteration process, we also examine the relative errors of Lagrange multipliers:

$$(L_1^k, L_2^k, L_3^k) = \left(\frac{\|\lambda_1^k - \lambda_1^{k-1}\|_1}{\|\lambda_1^{k-1}\|_1}, \frac{\|\lambda_2^k - \lambda_2^{k-1}\|_1}{\|\lambda_2^{k-1}\|_1}, \frac{\|\lambda_3^k - \lambda_3^{k-1}\|_1}{\|\lambda_3^{k-1}\|_1}\right), \tag{25}$$

and the relative error in u^k:

$$R(u^k) = \frac{\|u^k - u^{k-1}\|_1}{\|u^{k-1}\|_1}. \tag{26}$$

In addition, the numerical energy is calculated by

$$E(u^k) = \int_\Omega \alpha(I)|\nabla u^k|dx + \int_\Omega \beta(I)|\nabla^2 u^k|dx + \lambda \int_\Omega (f_1 - f_2)u^k dx. \tag{27}$$

4.1. Evaluation criteria

In numerical experiments, the accuracy of segmentation is measured by Segmentation Accuracy (SA), F1-Score, Kappa coefficient (κ) and Jaccard Similarity (JS), which can be estimated by the stand confusion matrix as shown in Table 1. Generally speaking, the closer these values are to 1, the better the segmentation is.

Table 1: Confusion matrix

Confusion matrix		True	
		Positive	Negative
Predict	Positive	TP	FP
	Negative	FN	TN

① Segmentation Accuracy (SA):

$$\mathrm{SA} = \frac{\mathrm{TP}+\mathrm{TN}}{\mathrm{TP}+\mathrm{TN}+\mathrm{FP}+\mathrm{FN}}.$$

② F1-Score:

$$\text{F1-Score} = \frac{2\mathrm{PR}}{\mathrm{P}+\mathrm{R}} \quad \text{with } \mathrm{P} = \frac{\mathrm{TP}}{\mathrm{TP}+\mathrm{FP}}, \ \mathrm{R} = \frac{\mathrm{TP}}{\mathrm{TP}+\mathrm{FN}},$$

where P denotes Precision and R represents Recall.

③ Kappa coefficient (κ):

$$\kappa = \frac{\mathrm{SA}-\mathrm{P_e}}{1-\mathrm{P_e}} \quad \text{with } \mathrm{P_e} = \frac{(\mathrm{TP}+\mathrm{FN})(\mathrm{TP}+\mathrm{FP})+(\mathrm{FP}+\mathrm{TN})(\mathrm{FN}+\mathrm{TN})}{(\mathrm{TP}+\mathrm{TN}+\mathrm{FP}+\mathrm{FN})^2}.$$

④ Jaccard Similarity (JS):

$$\mathrm{JS}(S_1,S_2) = \frac{|S_1 \cap S_2|}{|S_1 \cup S_2|},$$

where S_1 is the region segmented by the Algorithm 1 and S_2 is the corresponding region of the ground truth.

4.2. Parameters discussion

Throughout all numerical experiments, the termination parameters are set as $K_{\max} = 400$ and $\varepsilon = 10^{-5}$ for all comparative algorithms. The experience-dependent penalty parameters r_1, r_2 in our model are fixed as $r_1 = 1$ and $r_2 = 2$, and the grid size is set as $h = 1$ for the differential operators in the first and second-order regularizers and $h = 5$ for the differential operators in $\alpha(I)$ and $\beta(I)$ to smooth out the small edges and structures in all experiments. The parameters λ and r_3 in our model are chosen empirically in each experiment, which play important roles in smoothing and regularizing the results.

On the other hand, the parameters including the regularization parameter λ, penalty parameter r and time step δ of the comparison algorithms are all adjusted to achieve accurate segmentation results, which are provided as follows:

① The active contour without edges (ACWE) model [2]: the regularization parameter is chosen from $\lambda \in [0.1,1]$, the time step is set as $\delta \in [0.1,0.5]$ and the ACWE model is also quite sensitive to the position of the initial contour.

② The fast global minimization of the active contour/snake (GMAC) model [8]: the regularization parameter λ is selected as [0.01,1] and the penalty parameter r is adjusted in the range [0.1,10].

③ The continuous max-flow (CMF) method [13]: the regularization parameter is chosen as $\lambda \in [0.1,0.5]$ and the time step of gradient projection is selected from $\delta \in [0.1,0.15]$.

④ The smoothed-dual (GMD) algorithm [11]: the regularization parameter is chosen from $\lambda \in [0.01,0.5]$ and the time step is selected from $\delta \in [0.001,0.01]$.

⑤ The efficient iterative thresholding (ICTM) method [5]: the regularization parameter is set as $\lambda \in [0.001,0.025]$ and the time step is $\delta \in [0.01,0.05]$.

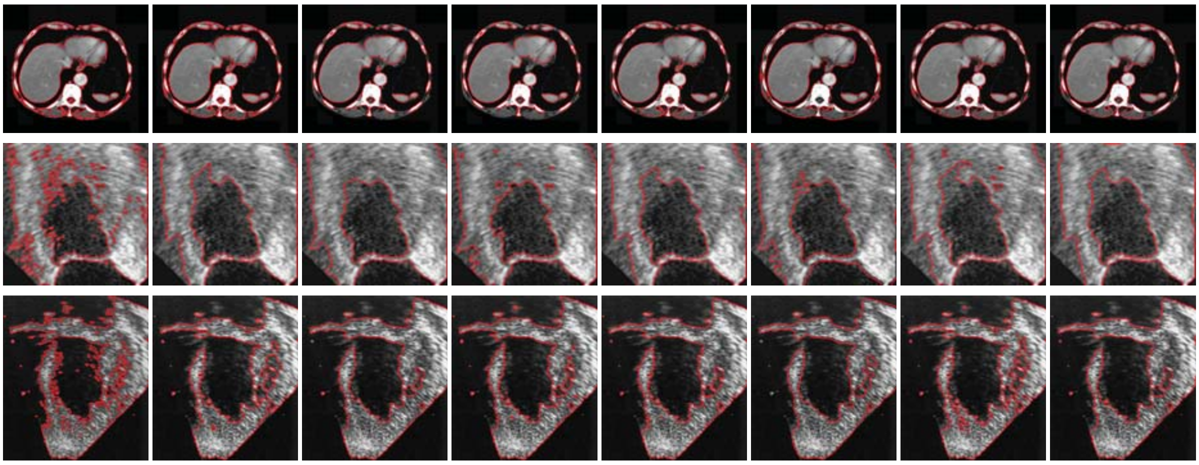

(a) ACWE (b) GMAC (c) CMF (d) GMD (e) ICTM (f) EMTV (g) T-ROF (h) Proposal

Figure 3: Labeling comparisons on images ‘Liver’ (Row 1), ‘Abdomina’ (Row 2) and ‘Ultrasound’ (Row 3). From left to right: (a)-(g) labeling results of ACWE, GMAC, CMF, GMD, ICTM, EMTV and T-ROF respectively; (h) our labeling result with the parameters $\lambda = 3$, $r_3 = 10$ for ‘Liver’, $\lambda = 3$, $r_3 = 0.5$ for ‘Abdomina’ and $\lambda = 3.5$, $r_3 = 10$ for ‘Ultrasound’, respectively.

⑥ The dual expectation-maximization TV (EMTV) algorithm [44]: the regularization parameter is $\lambda \in [1,50]$, penalty parameter is $r \in [1,100]$ and time step is $\delta \in [0.01,0.5]$.

⑦ The thresholded-ROF (T-ROF) method [22]: the regularization parameter is chosen from $\lambda \in [0.01,0.5]$ and the time step is selected from $\delta \in [0.01,0.03]$.

4.3. Numerical discretization

Without loss of generality, our images are 2-dimensional matrices of size $M \times N$. Let $\Omega = \{(i,j) : 0 \le i \le M, 0 \le j \le N\}$ be the discretized image domain and $u(i,j)$ denote an element of Euclidean space $\mathbb{R}^{M\times N}$. We first introduce the discrete forward and backward differential operators with the grid size h under periodic boundary condition as follows

$$\partial_x^+ u(i,j) = \begin{cases} (u(i+1,j) - u(i,j))/h, & \text{if } 1 \le i < M, \\ (u(1,j) - u(i,j))/h, & \text{if } i = M, \end{cases}$$

$$\partial_y^+ u(i,j) = \begin{cases} (u(i,j+1) - u(i,j))/h, & \text{if } 1 \le j < N, \\ (u(i,1) - u(i,j))/h, & \text{if } j = N, \end{cases}$$

$$\partial_x^- u(i,j) = \begin{cases} (u(i,j) - u(i-1,j))/h, & \text{if } 1 < i \le M, \\ (u(i,j) - u(M,j))/h, & \text{if } i = 1, \end{cases}$$

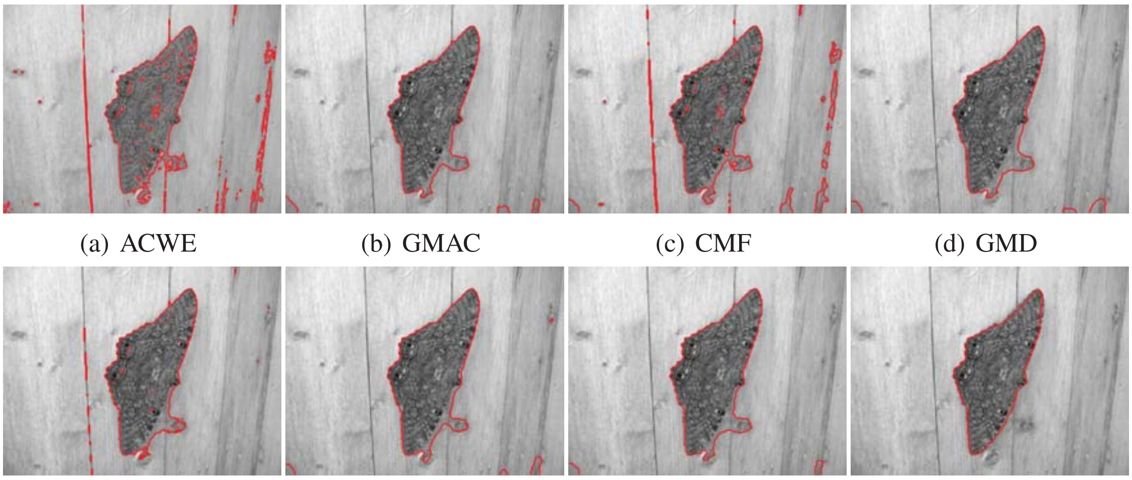

(a) ACWE (b) GMAC (c) CMF (d) GMD

(e) ICTM (f) EMTV (g) T-ROF (h) Our proposal

Figure 4: Segmentation comparison on image 'Butterfly'. From left to right: (a)-(g) segmentation results of ACWE, GMAC, CMF, GMD, ICTM, EMTV and T-ROF, respectively; (h) our segmentation result with the parameters $\lambda = 3$ and $r_3 = 70$.

$$\partial_y^- u(i,j) = \begin{cases} (u(i,j) - u(i,j-1))/h, & \text{if } 1 < j \leq N, \\ (u(i,j) - u(i,N))/h, & \text{if } j = 1. \end{cases}$$

Therefore, the discrete gradient operator $\nabla : \mathbb{R}^{M\times N} \to (\mathbb{R}^{M\times N})^2$ is denoted as

$$\nabla u(i,j) = \left(\partial_x^+ u(i,j), \partial_y^+ u(i,j)\right),$$

and the discrete divergence operator $\nabla\cdot : (\mathbb{R}^{M\times N})^2 \to \mathbb{R}^{M\times N}$ for $p = (p_1, p_2) \in (\mathbb{R}^{M\times N})^2$ is defined by

$$\nabla \cdot p(i,j) = \partial_x^- p_1(i,j) + \partial_y^- p_2(i,j),$$

and the discrete Laplacian operator $\triangle$ is defined based on the discrete gradient and divergence operator as

$$\triangle = \nabla \cdot \nabla = \partial_x^- \partial_x^+ + \partial_y^- \partial_y^+.$$

4.4. Computational complexity

In this subsection, we analyze the computational complexity of Algorithm 1. The main computational costs are spent on the calculation of $\{u, v, w, z\}$-subproblems, which are solved by the FFT and shrinkage operator. It is well-known the computational complexity of FFT and shrinkage operator are $\mathscr{O}[MN\log(MN)]$ and $\mathscr{O}(MN)$, respectively. Therefore, the total computational complexity of Algorithm 1 can be approximately given as $\mathscr{O}[MN\log(MN)]$ per iteration.

(a) ACWE (b) GMAC (c) CMF (d) GMD (e) ICTM

(f) EMTV (g) T-ROF (h) Our proposal (i) $\alpha(I)=0$ (j) $\beta(I)=0$

Figure 5: Segmentation comparison on image 'Aircraft'. From left to right: (a)-(g) segmentation results of ACWE, GMAC, CMF, GMD, ICTM, EMTV and T-ROF, respectively; (h) our segmentation result with the parameters $\lambda = 3$ and $r_3 = 30$; (i)-(j) our segmentation results with $\alpha(I) = 0$ and $\beta(I) = 0$, respectively.

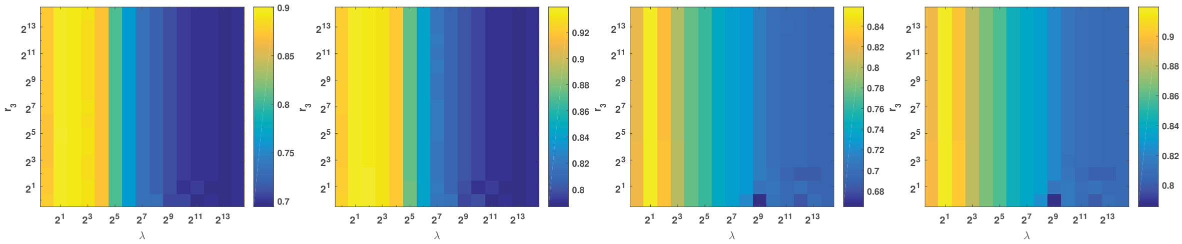

(a) Butterfly (JS) (b) Butterfly (κ) (c) Aircraft (JS) (d) Aircraft (κ)

Figure 6: The JS and κ of 'Butterfly' and 'Aircraft' by different parameters λ and r_3. From left to right: (a) Butterfly (JS); (b) Butterfly (κ); (c) Aircraft (JS); (d) Aircraft (κ).

5. Numerical Results

5.1. Image labeling experiments

In the first place, we compare the performance of our proposal (7) with other methods including the ACWE, GMAC, CMF, GMD, ICTM, EMTV and T-ROF models on two-phase labeling problems. We choose three medical images as examples, for which the values c_1, c_2 are predefined by the K-means algorithm. As shown in Figure 3, all the advanced methods outperform the ACWE model by providing labeling results with fewer outliers. Moreover, among these approaches, our method produces more consistent results. As can be observed, both the CMF and GMD models fail to identify the boundaries at the bottom part of the image 'Liver', which have similar intensity values as the liver. Moreover, the results of the GMD and T-ROF models contain too much meaningless scattered structures for the two ultrasound images, while the edges of the segmentation results from the GMAC and ICTM models are broken for the first ultrasound image. Although the EMTV and our model provide visually similar results, the boundaries of our results are smoother than the ones of the EMTV model.

Figure 7: Evaluation and comparison on natural images downloaded from the Weizmann segmentation dataset.

5.2. Image segmentation

We also test the proposed model (7) on image segmentation applications, where f_1 and f_2 are defined as

$$f_1 = (I - c_1)^2 \text{ and } f_2 = (I - c_2)^2$$

with c_1 and c_2 being updated iteratively from

$$c_1^k = \frac{\int_\Omega I v^k dx}{\int_\Omega v^k dx} \text{ and } c_2^k = \frac{\int_\Omega I(1 - v^k) dx}{\int_\Omega (1 - v^k) dx}.$$

We first apply all segmentation methods on two real images, ‘Butterfly’[1] and ‘Aircraft’[2]. The results of ‘Butterfly’ in Figure 4 demonstrate that the ACWE, CMF and ICTM methods can not smooth out some unwanted details, e.g., the chinks in the background, while the butterfly produced by the GMAC, GMD, EMTV, and T-ROF methods also present incorrect boundaries. As observed, our model gives the best segmentation result without redundant details and rough edges.

The image ‘Aircraft’ is a typical smooth image. As shown in Figure 5, only our model can accurately segment the aircraft from the background, while all comparison methods contain some undesired structures. Concretely, the ACWE, GMAC, CMF, GMD and EMTV methods segment the cloud into the phase of airplane, while the ICTM and T-ROF models fail to identify the entire plane tail. Also, we evaluate the performance of our model using only the spatially adaptive first-order regularizer and the second-order regularizer. By setting $\alpha(I) = 0$, our model reduces to a weighted high-order segmentation model, which can still produce reasonable segmentation results. However, letting $\beta(I) = 0$, the model becomes a weighted ACWE model, which results in some superfluous details and non-smoothed boundaries in the result. And the best segmentation results are still the ones achieved by our combined first and second-order regularization model.

---

[1] The image was downloaded from `http://www.wisdom.weizmann.ac.il/~vision/Seg_Evaluation_DB/`

[2] The image was downloaded from `https://www2.eecs.berkeley.edu/Research/Projects/CS/vision/bsds/`

(a) Given image (b) ACWE (c) GMAC (d) CMF (e) GMD

(f) ICTM (g) EMTV (h) T-ROF (i) Our proposal (j) Ground truth

Figure 8: Segmentation comparison on image '#11'. From left to right: (a) Given 300×247 image; (b)-(h) segmentation results of the ACWE, GMAC, CMF, GMD, ICTM, EMTV and T-ROF models, respectively; (i) our segmentation result with the parameters $\lambda = 10$ and $r_3 = 30$; (j) Ground truth.

5.3. Impact of parameters

There are two important parameters in our model, i.e., the regularization parameter λ and penalty parameter r_3. We track the values of JS and κ on 'Butterfly' and 'Aircraft' to illustrate the segmentation accuracy concerning different parameters. Figure 6 shows the JS and κ values of the two images with different combinations of λ and r_3, where λ and r_3 are selected from $(\lambda, r_3) \in \{2^{-1}, 2^0, \cdots, 2^{13}\} \times \{2^{-1}, 2^0, \cdots, 2^{13}\}$. It is obvious that both λ and r_3 affect the segmentation results. On one hand, λ is used to balance the contributions of the data fitting term and the regularization term. For large λ, the foreground contains many small structures and the boundaries are not neat enough, while for small λ, the model can not identify the boundaries of objects correctly. On the other hand, for the fixed regularization parameter λ, when the penalty parameter r_3 increases, the segmentation results tend to lose more details. Although it is necessary to manually tune these two parameters for different images, we can start from moderate values such as $\lambda = 3$ and $r_3 = 30$ and fine tune the results according to the above observations.

(a) Given image (b) ACWE (c) GMAC (d) CMF (e) GMD

(f) ICTM (g) EMTV (h) T-ROF (i) Our proposal (j) Ground truth

Figure 9: Segmentation comparison on image '#12'. From left to right: (a) Given 300×225 image; (b)-(h) segmentation results of the ACWE, GMAC, CMF, GMD, ICTM, EMTV and T-ROF models, respectively; (i) our segmentation result with the parameters $\lambda = 10$ and $r_3 = 30$; (j) Ground truth.

5.4. Segmentation on more natural images

To further verify the effectiveness and superiority of the proposed model, we test the methods on twelve natural images downloaded from the Weizmann segmentation dataset[3]. We select suitable parameters for each algorithm and fix them for these twelve images. Table 2 records the values of JS, SA, F1-Score and κ of each algorithm on every image. It can be seen that our proposal provides the highest mean and lowest variance compared to other approaches. Thus, our model is more reliable and stable with different images. The segmentation results of two examples from these twelve images (i.e., '#11' and '#12') are displayed in Figure 8 and Figure 9. We observe that our proposal can not only identify the correct boundaries of the chains but also distinguish the sharps and corners correctly. The GMAC, CMF, and GMD methods segment the incorrect boundaries of coconut trees in Figure 9, while ACWE, ICTM, and EMTV provide too much undesired scattered structures in the results. Besides, the results of the image '#11' illustrate that the ICTM model is more sensitive to parameters compared to other methods.

---

[3] `http://www.wisdom.weizmann.ac.il/~vision/Seg_Evaluation_DB`

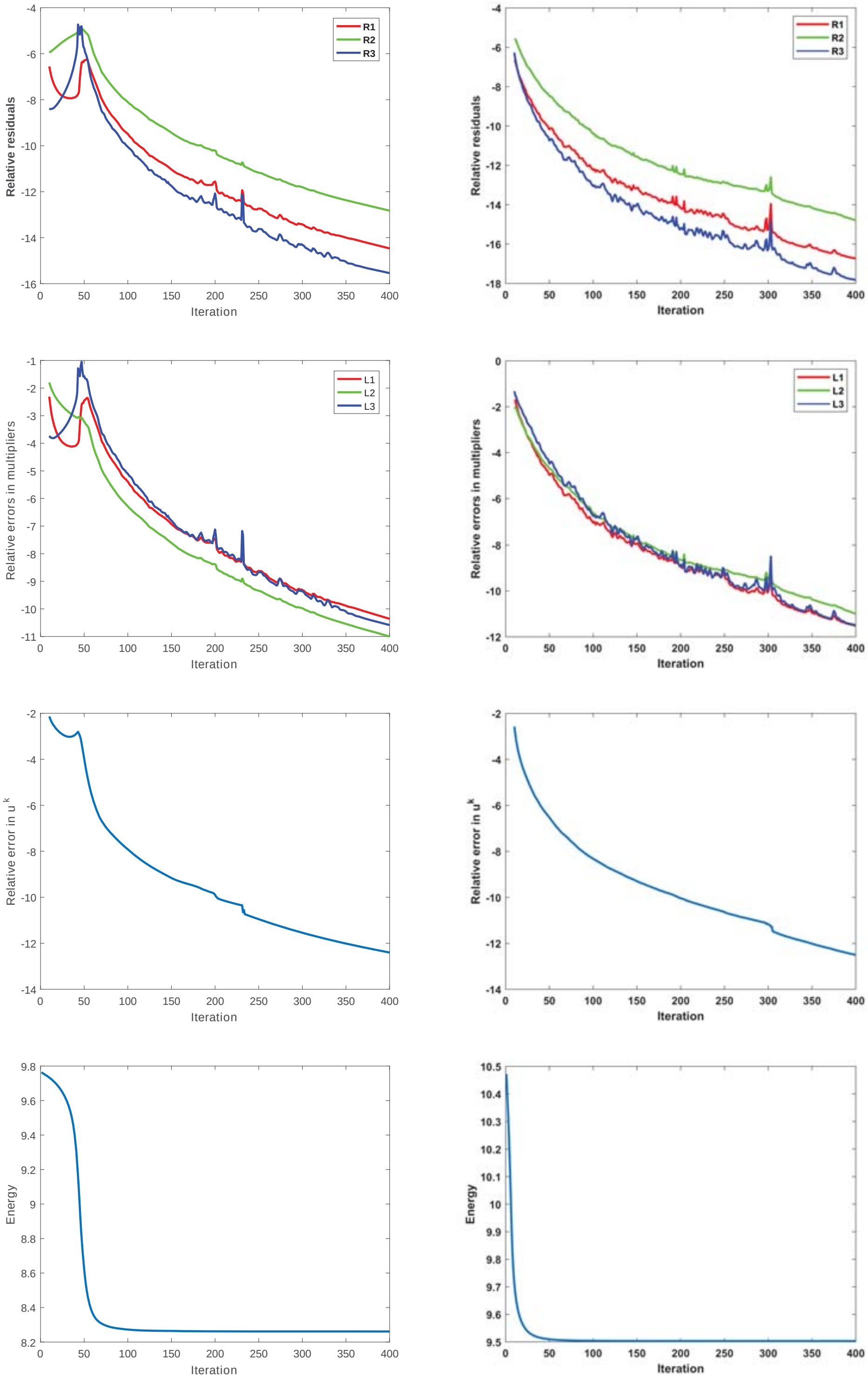

(a) Liver (b) #11

Figure 10: The plots of relative residuals, relative errors in Lagrange multipliers, relative error in u^k, and numerical energy of image ‘Liver’ and ‘#11’.

Table 2: The JS, SA, F1-Score and κ values on twelve natural images of the ACWE, GMAC, CMF, GMD, ICTM, EMTV, T-ROF and our proposal.

Criteria	JS								SA							
Images	ACWE	GMAC	CMF	GMD	ICTM	EMTV	T-ROF	OUR	ACWE	GMAC	CMF	GMD	ICTM	EMTV	T-ROF	OUR
#1	0.7167	0.9457	0.9450	0.9668	0.9481	0.9500	0.9426	0.9571	0.9528	0.9933	0.9933	0.9960	0.9937	0.9939	0.9929	0.9947
#2	0.9890	0.9895	0.9855	0.9857	0.9894	0.9910	0.9900	0.9897	0.9938	0.9942	0.9919	0.9920	0.9941	0.9950	0.9944	0.9943
#3	0.9551	0.9498	0.9476	0.9502	0.9538	0.9342	0.9506	0.9545	0.9939	0.9932	0.9928	0.9932	0.9937	0.9911	0.9933	0.9938
#4	0.8803	0.9066	0.9047	0.8993	0.8942	0.9072	0.9009	0.9001	0.9925	0.9941	0.9939	0.9936	0.9933	0.9940	0.9937	0.9937
#5	0.8284	0.8416	0.8179	0.8267	0.8356	0.8560	0.8293	0.8398	0.9763	0.9781	0.9748	0.9760	0.9773	0.9800	0.9762	0.9778
#6	0.8881	0.9216	0.9124	0.9179	0.9157	0.8625	0.9076	0.9098	0.9453	0.9611	0.9560	0.9592	0.9585	0.9327	0.9545	0.9556
#7	0.9934	0.9935	0.9878	0.9928	0.9936	0.9854	0.9849	0.9929	0.9981	0.9981	0.9965	0.9980	0.9982	0.9958	0.9957	0.9980
#8	0.9700	0.9725	0.9708	0.9717	0.9735	0.9713	0.9692	0.9718	0.9917	0.9924	0.9919	0.9922	0.9927	0.9920	0.9914	0.9922
#9	0.9508	0.9671	0.9612	0.9638	0.9643	0.9821	0.9657	0.9645	0.9904	0.9936	0.9924	0.9929	0.9930	0.9965	0.9933	0.9931
#10	0.9257	0.9303	0.9370	0.9222	0.9285	0.9451	0.9214	0.9271	0.9969	0.9971	0.9974	0.9967	0.9970	0.9977	0.9967	0.9969
#11	0.7960	0.8371	0.8065	0.8443	0.3116	0.7702	0.8196	0.8184	0.9699	0.9760	0.9715	0.9770	0.6913	0.9661	0.9734	0.9732
#12	0.6763	0.3288	0.4017	0.3393	0.6907	0.6836	0.7505	0.7541	0.9600	0.7713	0.8352	0.7957	0.9617	0.9610	0.9691	0.9696
Mean	0.8808	0.8820	0.8815	0.8817	0.8666	0.9032	0.9110	**0.9150**	0.9801	0.9702	0.9740	0.9719	0.9620	0.9830	0.9854	**0.9861**
Variance	0.0112	0.0329	0.0263	0.0320	0.0376	0.0091	0.0056	**0.0056**	0.0004	0.0040	0.0021	0.0032	0.0075	0.0004	0.0002	**0.0002**
Criteria	F1-Score								κ							
Images	ACWE	GMAC	CMF	GMD	ICTM	EMTV	T-ROF	OUR	ACWE	GMAC	CMF	GMD	ICTM	EMTV	T-ROF	OUR
#1	0.8350	0.9721	0.9717	0.9831	0.9734	0.9744	0.9705	0.9781	0.8082	0.9683	0.9680	0.9808	0.9698	0.9709	0.9665	0.9751
#2	0.9944	0.9947	0.9927	0.9928	0.9947	0.9955	0.9950	0.9948	0.9875	0.9882	0.9836	0.9839	0.9880	0.9898	0.9887	0.9884
#3	0.9770	0.9743	0.9731	0.9744	0.9764	0.9660	0.9747	0.9767	0.9735	0.9703	0.9689	0.9705	0.9727	0.9609	0.9708	0.9732
#4	0.9364	0.9510	0.9499	0.9470	0.9441	0.9513	0.9479	0.9474	0.9324	0.9478	0.9467	0.9436	0.9406	0.9481	0.9445	0.9441
#5	0.9062	0.9140	0.8998	0.9051	0.9104	0.9224	0.9067	0.9129	0.8927	0.9015	0.8855	0.8915	0.8975	0.9110	0.8931	0.9003
#6	0.9407	0.9592	0.9542	0.9572	0.9560	0.9262	0.9516	0.9528	0.8902	0.9220	0.9119	0.9182	0.9169	0.8648	0.9087	0.9110
#7	0.9967	0.9967	0.9939	0.9964	0.9968	0.9926	0.9924	0.9964	0.9953	0.9955	0.9914	0.9950	0.9955	0.9897	0.9894	0.9950
#8	0.9848	0.9861	0.9852	0.9856	0.9866	0.9854	0.9843	0.9857	0.9791	0.9808	0.9796	0.9802	0.9815	0.9800	0.9785	0.9803
#9	0.9748	0.9833	0.9802	0.9816	0.9818	0.9910	0.9826	0.9820	0.9689	0.9793	0.9755	0.9772	0.9775	0.9888	0.9784	0.9777
#10	0.9614	0.9639	0.9675	0.9595	0.9629	0.9718	0.9591	0.9622	0.9598	0.9624	0.9661	0.9578	0.9614	0.9706	0.9574	0.9606
#11	0.8864	0.9113	0.8929	0.9156	0.4752	0.8702	0.9009	0.9002	0.8693	0.8975	0.8767	0.9024	0.3266	0.8511	0.8856	0.8849
#12	0.8069	0.4948	0.5732	0.5067	0.8171	0.8121	0.8575	0.8598	0.7854	0.3846	0.4872	0.4035	0.7965	0.7911	0.8405	0.8431
Mean	0.9334	0.9251	0.9279	0.9254	0.9146	0.9466	0.9519	**0.9541**	0.9202	0.9082	0.9118	0.9087	0.8937	0.9347	0.9418	**0.9445**
Variance	0.0040	0.0191	0.0136	0.0182	0.0216	0.0032	0.0018	**0.0018**	0.0050	0.0283	0.0194	0.0265	0.0349	0.0043	0.0023	**0.0023**

5.5. Numerical convergence

To check whether the iteration of the ADMM-based algorithm converges to a saddle-point of the augmented Lagrangian functional, we track the decay of relative residuals (24), relative errors of the Lagrange multipliers (25), the relative error of the iterative $R(u^k)$ (26) and the numerical energy $E(u^k)$ (27). In Figure 10, we present the plots of these quantities versus iterations on the image 'Liver' and '#11' in the log-scale. We observe that: 1) the plots demonstrate the convergence of the iterative process and show that the iterations converge to certain saddle-point numerically; 2) the plots also verify the efficiency and stability of the ADMM-based algorithm, which converges fast with a few hundred of iterations for both images.

6. Extension to Two-stage Image Segmentation Framework

In this section, we further apply the weighted bounded Hessian variational model in the two-stage segmentation formulation to deal with multi-phase segmentation problems. The two-stage segmentation method can provide a good understanding of the link between image segmentation and image restoration. In first stage, we find a smooth image u from the blurry and noisy image I to facilitate the segmentation by solving the following restoration problem

$$\min_{u} \int_{\Omega} \alpha(x)|\nabla u|dx + \int_{\Omega} \beta(x)|\nabla^2 u|dx + \frac{\lambda}{2}\int_{\Omega}(Ku-I)^2 dx. \tag{28}$$

Because the observed image is noisy and blurry, inaccurate boundaries may be located by estimating $\alpha(x)$ and $\beta(x)$ using (12). Thus, we define $\alpha(x)$ and $\beta(x)$ as functions of u to boost the restoration result, i.e.,

$$\alpha(u)=\left|\nabla\frac{1}{\sqrt{1+|\nabla u|^2}}\right| \text{ and } \beta(u)=\frac{1}{\sqrt{1+|\nabla u|^2}},$$

which are updated dynamically in the iterative process. As the quality of u becomes better and better, $\alpha(u)$ and $\beta(u)$ can locate the boundaries more accurately.

Similarly, the minimization problem (28) can be solved by the efficient ADMM-based algorithm. By introducing two auxiliary variables v and w, we reformulate (28) into an equivalent constrained minimization problem as follows

$$\begin{aligned}&\min_{u,v,w}\int_\Omega \alpha(u)|v|dx+\int_\Omega \beta(u)|w|dx+\frac{\lambda}{2}\int_\Omega (Ku-I)^2dx\\ &\text{s.t. } v=\nabla u,\ w=\nabla^2 u.\end{aligned} \tag{29}$$

Thus, the associated augmented Lagrangian functional for the constrained optimization problem can be defined as

$$\begin{aligned}\mathscr{L}(u,v,w;\Lambda_1,\Lambda_2)=&\int_\Omega \alpha(u)|v|dx+\int_\Omega \beta(u)|w|dx+\frac{\lambda}{2}\int_\Omega (Ku-I)^2dx\\ &+\frac{r_1}{2}\int_\Omega \big(v-\nabla u+\frac{\lambda_1}{r_1}\big)^2dx+\frac{r_2}{2}\int_\Omega \big(w-\nabla^2 u+\frac{\lambda_2}{r_2}\big)^2dx,\end{aligned} \tag{30}$$

where λ_1, λ_2 are the Lagrange multipliers, and r_1, r_2 denote the positive penalty parameters. During each iteration, we tend to sequentially minimize over variables u, v, w and update the Lagrange multipliers λ_1, λ_2 through a standard dual-ascent rule. Since each subproblem can be solved in a similar way as previous, we omit the details and simply present the subproblems in Algorithm 2.

Once the smooth solution u is obtained, the segmentation can be realized using proper thresholds ρ. We can select the thresholds using automatic clustering algorithms such as K-means [45] and a more advanced fuzzy c-means method [46]. Alternatively, users can try different values of thresholds to get satisfactory results. Note that one merit of the two-stage segmentation framework is there is no need to recompute the image u when we change the thresholds. One can just use the new thresholds to obtain the segmentation result.

6.1. Experimental results

In this subsection, we evaluate the performance of our two-stage weighted Hessian model by comparing it with other established two-stage segmentation methods. To guarantee the fairness of experimental comparison, the parameters are chosen by trials to obtain the best results for the respective methods. We first give the following two remarks concerning the parameters and stopping criteria:

Algorithm 2 The ADMM-based algorithm for the two-stage bounded Hessian model

```
Input: Degraded image $I$, regularization parameter $\lambda$, penalty factor $r_1, r_2$, maximum iteration $K_{\max}$, and stopping threshold $\varepsilon$
Initialize: $u^0 = I$, and $v^0 = \lambda_1^0 = \lambda_2^0 = 0$, set $k = 0$
/*            Stage I            */
while (not converged and $k \le K_{\max}$) do
    Compute $u^{k+1}$ with fixed $v^k$, $w^k$ and $\lambda_1^k, \lambda_2^k$ from:
        $u^{k+1} = \arg\min_u \frac{r_1}{2}\int_\Omega (\nabla u - v^k - \frac{\lambda_1^k}{r_1})^2 dx + \frac{r_2}{2}\int_\Omega (\nabla^2 u - w^k - \frac{\lambda_2^k}{r_2})^2 dx + \frac{\lambda}{2}\int_\Omega (Ku - I)^2 dx,$
    which can be solved by FFT.
    Update $\alpha(u^{k+1})$ and $\beta(u^{k+1})$ using the latest $u^{k+1}$ from
        $\alpha(u^{k+1}) = \left|\nabla \frac{1}{\sqrt{1+|\nabla u^{k+1}|^2}}\right|$ and $\beta(u^{k+1}) = \frac{1}{\sqrt{1+|\nabla u^{k+1}|^2}}.$
    Compute $v^{k+1}$ with fixed $u^{k+1}$, $\alpha(u^{k+1})$ and $\lambda_1^k$ from:
        $v^{k+1} = \arg\min_v \int_\Omega \alpha(u^{k+1})|v| dx + \frac{r_1}{2}\int_\Omega \big(v - \nabla u^{k+1} + \frac{\lambda_1^k}{r_1}\big)^2 dx,$
    which can be solved by the shrinkage operator.
    Compute $w^{k+1}$ with fixed $u^{k+1}$, $\beta(u^{k+1})$ and $\lambda_2^k$ from:
        $w^{k+1} = \arg\min_w \int_\Omega \beta(u^{k+1})|w| dx + \frac{r_2}{2}\int_\Omega \big(w - \nabla^2 u^{k+1} + \frac{\lambda_2^k}{r_2}\big)^2 dx,$
    which can be solved by the shrinkage operator.
    Update $\lambda_1^{k+1}, \lambda_2^{k+1}$ with $u^{k+1}$, $v^{k+1}$ and $w^{k+1}$ from:
        $\lambda_1^{k+1} = \lambda_1^k + r_1(v^{k+1} - \nabla u^{k+1}),$
        $\lambda_2^{k+1} = \lambda_2^k + r_2(w^{k+1} - \nabla^2 u^{k+1}).$
    Check the convergence condition:
        $\|u^{k+1} - u^k\|_1 \le \varepsilon \|u^k\|_1.$
end while
/*            Stage II            */
Use the K-means to choose the thresholds and obtain the segmentation result.
```


(a) Given image (b) TSMS (c) TSEE (d) T-ROF (e) $\rho = 0.4036$ (f) $\rho^U = 0.2$ (g) $\rho^U = 0.5$

Figure 11: Comparison of the kidney vascular system segmentation. (a) Given 255×255 image; (b)-(d) segmentations of TSMS, TSEE and T-ROF; (e)-(g) our segmentation using $\lambda = 0.01$ and thresholds $\rho = 0.4036$, $\rho^U = 0.2$ and 0.5, respectively.

① We use the K-means to estimate the thresholds ρ for the two-stage Mumford-Shah (TSMS) model in [15], two-stage Euler's elastica (TSEE) model in [19], thresholded-ROF (T-ROF) model in [22] and our proposal. In numerical experiments, the penalty parameters are fixed as $r_1 = 1$, $r_2 = 2$ and the mesh size is set as $h = 5$ for all examples. The regularization parameter λ is chosen empirically to guarantee segmentation performance.

② The iteration of all the two-stage segmentation methods are terminated using the same criterion such that either the relative error satisfies

$$R(u^{k+1}) = \frac{\|u^{k+1} - u^k\|_1}{\|u^k\|_1} \leq \varepsilon$$

with $\varepsilon = 10^{-4}$ or the maximum iteration number (i.e., $K_{\max} = 400$) is reached.

In Figure 11, we use an example to discuss the influences of the thresholds to final segmentation results. Figure 11(a) is a given magnetic resonance angiography kidney image. Figure 11(b)-(d) are the results of the TSMS, TSEE, and T-ROF models, while Figure 11(e)-(g) are our segmentation results with the threshold obtained by the K-means method ($\rho = 0.4036$) and the thresholds chosen by users ($\rho^U = 0.2$ and 0.5). As shown, visually similar segmentation results are obtained by these four two-stage segmentation methods with the threshold automatically computed by the K-means. The segmentation results in Figure 11(f) and (g) illustrate that too large threshold may lead to discontinuous segmentation results with important structures missing, and too small threshold results in retaining unnecessary details and segmenting incorrect boundaries. Besides, we can observe that the two-stage method can reveal different meaningful features in the image by choosing different thresholds, which can be done without recomputing the first stage. In the following, we use the K-means to estimate the thresholds automatically, which usually can provide moderate satisfactory results.

We generate the test images using two different kinds of blurring such that Figure 12 (a) and Figure 13 (a) are degraded by motion blur kernel [fspecial ('motion', [90,15])] and Gaussian blur kernel [fspecial ('gaussian', [15,15], 15)], respectively. Both images are introduced with the Gaussian noise with a mean 0 and a standard deviation of $\sigma = 10$. As shown in Figure 12, both the TSMS and T-ROF models erroneously segment the rectangles into the same phase, which results in bad evaluation values (e.g., JS, F1-score and κ) as shown in Table 3. Although

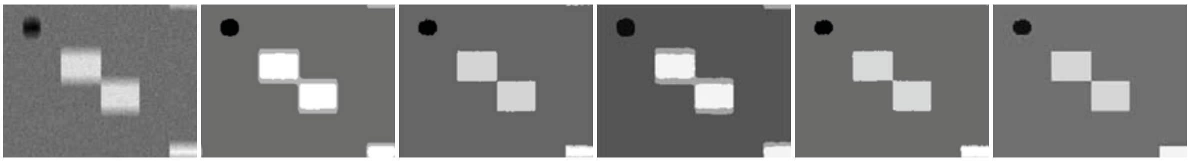

(a) Degraded image (b) TSMS (c) TSEE (d) T-ROF (e) Our proposal (f) Ground truth

Figure 12: Comparison of the four-phase synthetic image segmentation. (a) Given degraded image (184 × 234); (b)-(d) segmentation of the TSMS, TSEE and T-ROF model; (e) our segmentation result with $\lambda = 0.05$; (f) ground truth.

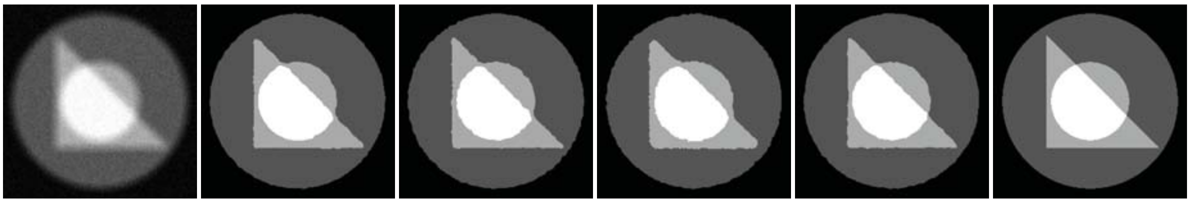

(a) Degraded image (b) TSMS (c) TSEE (d) T-ROF (e) Our proposal (f) Ground truth

Figure 13: Comparison of the four-phase synthetic image segmentation. (a) Given degraded image (256 × 256); (b)-(d) segmentation result of the TSMS, TSEE and T-ROF model; (e) our segmentation result with $\lambda = 0.1$; (f) ground truth.

Table 3: Evaluation results of the comparative methods in Figure 12 and Figure 13.

Images	Methods	First-phase				Second-phase				Third-phase			
		JS	SA	F1-Score	κ	JS	SA	F1-Score	κ	JS	SA	F1-Score	κ
Figure 12	TSMS	0.1683	0.9214	0.2882	0.2601	0.1337	0.9294	0.2359	0.2194	0.9727	0.9751	0.9862	0.8618
	TSEE	0.8743	0.9887	0.9329	0.9267	0.6782	0.9961	0.8082	0.8063	0.9876	0.9886	0.9937	0.9328
	T-ROF	0.1937	0.9143	0.3246	0.2849	0.1383	0.9352	0.2430	0.2269	0.9598	0.9633	0.9795	0.8069
	Our proposal	**0.8915**	**0.9904**	**0.9426**	**0.9374**	**0.7642**	**0.9971**	**0.8663**	**0.8649**	**0.9888**	**0.9897**	**0.9943**	**0.9389**
Figure 13	TSMS	0.9487	0.9945	0.9737	0.9706	0.9756	0.9977	0.9877	0.9864	0.9670	0.9852	0.9832	0.9700
	TSEE	0.9542	0.9951	0.9765	0.9738	0.9777	0.9978	0.9887	0.9875	0.9675	0.9854	0.9835	0.9704
	T-ROF	0.9013	0.9891	0.9481	0.9420	0.9535	0.9954	0.9762	0.9737	0.9548	0.9797	0.9769	0.9588
	Our proposal	**0.9552**	**0.9952**	**0.9771**	**0.9744**	**0.9840**	**0.9985**	**0.9919**	**0.9911**	**0.9682**	**0.9858**	**0.9839**	**0.9711**

the TSEE model provides visually satisfactory four-phase segmentation results, there presents some unexpected artifacts on the boundaries. Due to the spatially adaptive weights, our proposal can identify the boundaries more accurately, which is further convinced by the indexes in Table 3. Similar segmentation results are achieved on the other four-phase image in Figure 13. As shown, our model produces better segmentation result with more accurate boundaries than the competing methods. Moreover, the evaluation indexes recorded in Table 3 also demonstrate the effectiveness and superiority of our proposal.

Finally, we test our two-stage model on two brain MRI images from the BrainWeb dataset[4]. Figure 14 (a) is contaminated by the Gaussian noise with a mean 0 and a standard deviation of $\sigma = 10$, and Figure 15 (a) is degraded by the Gaussian blur kernel [fspecial ('gaussian', [3,3], 3)] and the Gaussian noise with a mean 0 and a standard deviation of $\sigma = 5$. We display the

---

[4] `https://brainweb.bic.mni.mcgill.ca/`

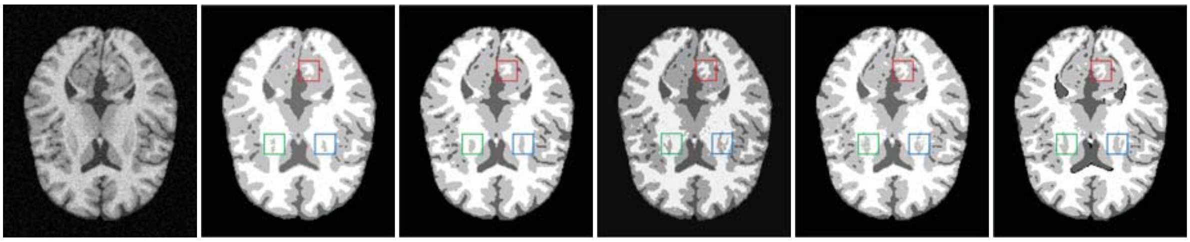

(a) Noisy image (b) TSMS (c) TSEE (d) T-ROF (e) Our proposal (f) Ground truth

Figure 14: Comparison on four-phase brain MRI image segmentation. (a) Given noisy image (217×181); (b)-(d) segmentations of TSMS, TSEE and T-ROF; (e) our segmentation with $\lambda = 0.05$; (f) ground truth.

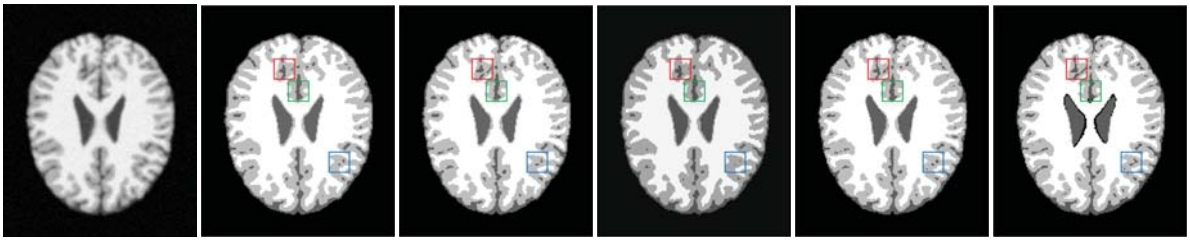

(a) Blurry image (b) TSMS (c) TSEE (d) T-ROF (e) Our proposal (f) Ground truth

Figure 15: Comparison on four-phase brain MRI image segmentation. (a) Given noisy and blurry image (217×181); (b)-(d) segmentations of TSMS, TSEE and T-ROF; (e) our segmentation with $\lambda = 0.2$; (f) ground truth.

Table 4: Evaluation results of the comparative methods in Figure 14 and Figure 15.

Images	Methods	CF				GM				WM			
		JS	SA	F1-Score	κ	JS	SA	F1-Score	κ	JS	SA	F1-Score	κ
Figure 14	TSMS	0.8315	0.9561	0.9080	0.8791	0.8616	0.9705	0.9257	0.9073	0.8348	0.9856	0.9100	0.9022
	TSEE	0.8403	0.9587	0.9132	0.8862	0.8719	0.9729	0.9316	0.9147	0.8353	0.9855	0.9103	0.9024
	T-ROF	0.8420	0.9583	0.9142	0.8867	0.8827	0.9756	0.9377	0.9225	0.7789	0.9807	0.8757	0.8652
	Our proposal	**0.8625**	**0.9647**	**0.9262**	**0.9030**	**0.8927**	**0.9775**	**0.9433**	**0.9293**	**0.8435**	**0.9865**	**0.9151**	**0.9078**
Figure 15	TSMS	0.8339	0.9694	0.9094	0.8910	0.9359	0.9843	0.9669	0.9566	0.7969	0.9855	0.8870	0.8792
	TSEE	0.8328	0.9691	0.9088	0.8902	0.9324	0.9835	0.9650	0.9542	0.8016	0.9859	0.8899	0.8824
	T-ROF	0.7912	0.9601	0.8834	0.8593	0.9169	0.9795	0.9566	0.9432	0.7266	0.9803	0.8417	0.8312
	Our proposal	**0.8462**	**0.9719**	**0.9167**	**0.8998**	**0.9363**	**0.9844**	**0.9671**	**0.9569**	**0.8050**	**0.9863**	**0.8920**	**0.8847**

segmentation results of the TSMS, TSEE, T-ROF, and our model in Figures 14 and 15, where our model produces more accurate results than the others, especially the regions inside the red, green and blue box. We also compare the results in terms of JS, SA, F1-Score and κ in Table 4. As can be observed, our model gives the best segmentation results for all three tissues, i.e., cerebrospinal fluid (CF), gray matter (GM) and white matter (WM).

7. Conclusions

In this paper, we proposed a variational model in the space of functions of bounded Hessian to overcome the shortage of TV regularizer in segmenting natural images containing both flat regions and slanted regions. Instead of using constant parameters, we estimated the spatial varying parameters in advance according to the edge information of images. The resulting nonsmooth optimization problem was efficiently solved by the ADMM-based algorithm. Because of the convexity, our model performed more stable concerning parameters and initializations. Numerical experiments implemented on natural images demonstrated the efficacious and accurate performance of our proposed method by comparing with several advanced segmentation methods. We also extended the weighted bounded Hessian regularizer to the two-stage segmentation framework to deal with noisy and blurry images, which also achieved state-of-the-art results.

As far as future work is concerned, an automatic way to select λ in the proposed model would be useful. We may use the bi-level learning scheme to estimate the value of λ from the dataset [47] or use the parameter-free fitting term in [48]. Moreover, we would like to investigate the performance of the weighted bounded Hessian regularizer on other image processing tasks such as super-resolution imaging, Retinex, etc.

Acknowledgements

The authors would like to thank Dr. Gu and Prof. Cai for sharing the MATLAB code of image segmentation and the reviewers for providing us numerous valuable suggestions to revise this paper. The work is partially supported by the National Natural Science Foundation of China No. 11701418, Major Science and Technology Project of Tianjin 18ZXRHSY00160, and Recruitment Program of Global Young Expert. T. Zeng is supported by the National Science Foundation of China No. 11671002, CUHK start-up and CUHK DAG 4053342, RGC 14300219, and NSFC/RGC N_CUHK 415/19.

Appendix

Proof of Theorem 3.1

Proof. *According to Algorithm 1, we have*

$$\begin{cases} (-r_1\nabla\cdot\nabla + r_2\nabla^2\cdot\nabla^2 + r_3)u^{k+1} = -\nabla\cdot(r_1 w^k + \lambda_1^k) + \nabla^2\cdot(r_2 z^k + \lambda_2^k) + r_3 v^k + \lambda_3^k, \\ r_3(v^{k+1} - u^{k+1}) + \lambda_3^k + \lambda(f_1 - f_2) \ni 0, \\ \alpha(I)s^{k+1} + r_1(w^{k+1} - \nabla u^{k+1}) + \lambda_1^k \ni 0, \ s^{k+1} \in \partial|w^{k+1}|, \\ \beta(I)p^{k+1} + r_2(z^{k+1} - \nabla^2 u^{k+1}) + \lambda_2^k \ni 0, \ p^{k+1} \in \partial|z^{k+1}|, \\ \lambda_1^{k+1} = \lambda_1^k + r_1(w^{k+1} - \nabla u^{k+1}), \\ \lambda_2^{k+1} = \lambda_2^k + r_2(z^{k+1} - \nabla^2 u^{k+1}), \\ \lambda_3^{k+1} = \lambda_3^k + r_3(v^{k+1} - u^{k+1}). \end{cases} \tag{31}$$

Based on the assumption $\lambda_1^{k+1} - \lambda_1^k \to 0$ *as* $k \to \infty$, *we have* $\lim\limits_{k\to\infty}(w^k - \nabla u^k) \to 0$. *Moreover, we can obtain* $w^{k+1} - w^k = w^{k+1} - \nabla u^{k+1} + \nabla u^{k+1} - \nabla u^k + \nabla u^k - w^k$ *and deduce* $\lim\limits_{k\to\infty}(w^{k+1} - w^k) \to 0$ *by* $u^{k+1} - u^k \to 0$. *Similarly, there is* $\lim\limits_{k\to\infty}(z^k - \nabla^2 u^k) \to 0$ *with the assumption* $\lambda_2^{k+1} -$

$\lambda_2^k \to 0$ *as* $k \to \infty$, *which immediately gives* $\lim\limits_{k\to\infty}(z^{k+1} - z^k) \to 0$. *Due to* $\lambda_3^{k+1} - \lambda_3^k \to 0$ *and* $u^{k+1} - u^k \to 0$ *as* $k \to \infty$, *we also have* $\lim\limits_{k\to\infty}(v^k - u^k) \to 0$, *which deduces that* $\lim\limits_{k\to\infty}(v^{k+1} - v^k) \to 0$. *Thus, the sequence* $\{(u^k, v^k, w^k, z^k; \lambda_1^k, \lambda_2^k, \lambda_3^k)\}_{k\in\mathbb{N}}$ *is uniformly bounded in* Ω.

Moreover, let $(u^*, v^*, w^*, z^*; \lambda_1^*, \lambda_2^*, \lambda_3^*)$ *be a cluster point of the generated sequence* $\{(u^k, v^k, w^k, z^k; \lambda_1^k, \lambda_2^k, \lambda_3^k)\}_{k\in\mathbb{N}}$ *by the ADMM-based Algorithm 1. Thus, there exists a weakly convergent subsequence denoted by* $\{(u^{k_\ell}, v^{k_\ell}, w^{k_\ell}, z^{k_\ell}; \lambda_1^{k_\ell}, \lambda_2^{k_\ell}, \lambda_3^{k_\ell})\}_{\ell\in\mathbb{N}}$ *converging to the limite point* $(u^*, v^*, w^*, z^*; \lambda_1^*, \lambda_2^*, \lambda_3^*)$. *Analogously, due to* $w^{k_\ell} \to w^*$, $z^{k_\ell} \to z^*$ *a.e. in* Ω *as* $\ell \to \infty$ *and* $s^{k_\ell} \in \partial|w^{k_\ell}|$, $p^{k_\ell} \in \partial|z^{k_\ell}|$, *there exists a subsequence of* $\{s^{k_\ell}\}_{\ell\in\mathbb{N}}$ *and* $\{p^{k_\ell}\}_{\ell\in\mathbb{N}}$ *that converges weakly to* $s^* \in \partial|w^*|$ *and* $p^* \in \partial|z^*|$, *respectively.*

The subsequence $\{(u^{k_\ell}, v^{k_\ell}, w^{k_\ell}, z^{k_\ell}; \lambda_1^{k_\ell}, \lambda_2^{k_\ell}, \lambda_3^{k_\ell})\}_{\ell\in\mathbb{N}}$ *satisfies the first-order optimality conditions* (31), *i.e.,*

$$\begin{cases}
(-r_1\nabla\cdot\nabla + r_2\nabla^2\cdot\nabla^2 + r_3)u^{k_\ell+1} = -\nabla\cdot(r_1 w^{k_\ell} + \lambda_1^{k_\ell}) + \nabla^2\cdot(r_2 z^{k_\ell} + \lambda_2^{k_\ell}) + r_3 v^{k_\ell} + \lambda_3^{k_\ell},\\
r_3(v^{k_\ell+1} - u^{k_\ell+1}) + \lambda_3^{k_\ell} + \lambda(f_1 - f_2) \ni 0,\\
\alpha(I)s^{k_\ell+1} + r_1(w^{k_\ell+1} - \nabla u^{k_\ell+1}) + \lambda_1^{k_\ell} \ni 0,\\
\beta(I)p^{k_\ell+1} + r_2(z^{k_\ell+1} - \nabla^2 u^{k_\ell+1}) + \lambda_2^{k_\ell} \ni 0,\\
\lambda_1^{k_\ell+1} = \lambda_1^{k_\ell} + r_1(w^{k_\ell+1} - \nabla u^{k_\ell+1}),\\
\lambda_2^{k_\ell+1} = \lambda_2^{k_\ell} + r_2(z^{k_\ell+1} - \nabla^2 u^{k_\ell+1}),\\
\lambda_3^{k_\ell+1} = \lambda_3^{k_\ell} + r_3(v^{k_\ell+1} - u^{k_\ell+1}).
\end{cases}$$

Taking the limit from the convergent subsequence, i.e., letting $\ell \to \infty$, *we obtain*

$$\begin{cases}
\nabla\cdot\lambda_1^* - \nabla^2\cdot\lambda_2^* - \lambda_3^* = 0,\\
\lambda_3^* + \lambda(f_1 - f_2) = 0,\\
\alpha(I)s^* + \lambda_1^* = 0,\ s^* \in \partial|w^*|,\\
\beta(I)p^* + \lambda_2^* = 0,\ p^* \in \partial|z^*|,\\
w^* = \nabla u^*,\ z^* = \nabla^2 u^*,\ v^* = u^*,
\end{cases}$$

for almost every point in Ω. *This implies that the sequence* $\{(u^k, v^k, w^k, z^k; \lambda_1^k, \lambda_2^k, \lambda_3^k)\}_{k\in\mathbb{N}}$ *converges to the limit point* $(u^*, v^*, w^*, z^*; \lambda_1^*, \lambda_2^*, \lambda_3^*)$ *and satisfies the first-order optimality conditions.*

References

[1] D. Mumford, J. Shah, Optimal approximations by piecewise smooth functions and associated variational problems, Communications on Pure and Applied Mathematics 42 (5) (1989) 577–685.

[2] T. F. Chan, L. A. Vese, Active contours without edges, IEEE Transactions on Image Processing 10 (2) (2001) 266–277.

[3] L. A. Vese, T. F. Chan, A multiphase level set framework for image segmentation using the Mumford and Shah model, International Journal of Computer Vision 50 (3) (2002) 271–293.

[4] T. F. Chan, S. Esedoglu, M. Nikolova, Algorithms for finding global minimizers of image segmentation and denoising models, SIAM Journal on Applied Mathematics 66 (5) (2006) 1632–1648.

[5] D. Wang, H. Li, X. Wei, X.-P. Wang, An efficient iterative thresholding method for image segmentation, Journal of Computational Physics 350 (2017) 657–667.

[6] Y. Li, G. Cao, Q. Yu, X. Li, Fast and robust active contours model for image segmentation, Neural Processing Letters 49 (2) (2019) 431–452.

[7] M. Roberts, J. Spencer, Chan–Vese reformulation for selective image segmentation, Journal of Mathematical Imaging and Vision 61 (8) (2019) 1173–1196.

[8] X. Bresson, S. Esedoḡlu, P. Vandergheynst, J.-P. Thiran, S. Osher, Fast global minimization of the active contour/snake model, Journal of Mathematical Imaging and Vision 28 (2) (2007) 151–167.

[9] J. Lellmann, J. Kappes, Y. Jing, F. Becker, C. Schnorr, Convex multi-class image labeling by simplex-constrained total variation, in: Proceedings of International Conference on Scale Space and Variational Methods in Computer Vision, Springer, 2009, pp. 150–162.

[10] T. Pock, A. Chambolle, D. Cremers, H. Bischof, A convex approach for computing minimal partitions, in: Proceedings of Computer Society Conference on Computer Vision and Pattern Recognition, IEEE, 2009, pp. 810–817.

[11] E. Bae, J. Yuan, X.-C. Tai, Global minimization for continuous multiphase partitioning problems using a dual approach, International Journal of Computer Vision 92 (1) (2011) 112–129.

[12] Y. Gu, L.-L. Wang, X.-C. Tai, A direct approach toward global minimization for multiphase labeling and segmentation problems, IEEE Transactions on Image Processing 21 (5) (2012) 2399–2411.

[13] J. Yuan, E. Bae, X.-C. Tai, A study on continuous max-flow and min-cut approaches, in: Proceedings of Computer Society Conference on Computer Vision and Pattern Recognition, IEEE, 2010, pp. 2217–2224.

[14] J. Yuan, E. Bae, X.-C. Tai, Y. Boykov, A continuous max-flow approach to potts model, in: Proceedings of European Conference on Computer Vision, Springer, 2010, pp. 379–392.

[15] X. Cai, R. Chan, T. Zeng, A two-stage image segmentation method using a convex variant of the Mumford–Shah model and thresholding, SIAM Journal on Imaging Sciences 6 (1) (2013) 368–390.

[16] R. Chan, H. Yang, T. Zeng, A two-stage image segmentation method for blurry images with poisson or multiplicative gamma noise, SIAM Journal on Imaging Sciences 7 (1) (2014) 98–127.

[17] Y. Duan, H. Chang, W. Huang, J. Zhou, Z. Lu, C. Wu, The L_0 regularized Mumford-Shah model for bias correction and segmentation of medical images, IEEE Transactions on Image Processing 24 (11) (2015) 3927–3938.

[18] H. Chang, W. Huang, C. Wu, S. Huang, C. Guan, S. Sekar, K. K. Bhakoo, Y. Duan, A new variational method for bias correction and its applications to rodent brain extraction, IEEE Transactions on Medical Imaging 36 (3) (2016) 721–733.

[19] Y. Duan, W. Huang, J. Zhou, H. Chang, T. Zeng, A two-stage image segmentation method using Euler's elastica regularized Mumford-Shah model, in: Proceedings of International Conference on Pattern Recognition, IEEE, 2014, pp. 118–123.

[20] C. Liu, M. K.-P. Ng, T. Zeng, Weighted variational model for selective image segmentation with application to medical images, Pattern Recognition 76 (2018) 367–379.

[21] L. Chen, Y. Li, T. Zeng, Variational image restoration and segmentation with rician noise, Journal of Scientific Computing 78 (3) (2019) 1329–1352.

[22] X. Cai, R. Chan, C.-B. Sch$\ddot{o}$nlieb, G. Steidl, T. Zeng, Linkage between piecewise constant Mumford-Shah model and Rudin-Osher-Fatemi model and its virtue in image segmentation, SIAM Journal on Scientific Computing 41 (6) (2019) B1310–B1340.

[23] L.-C. Chen, G. Papandreou, I. Kokkinos, K. Murphy, A. L. Yuille, Deeplab: Semantic image segmentation with deep convolutional nets, atrous convolution, and fully connected CRFs, IEEE Transactions on Pattern Analysis and Machine Intelligence 40 (4) (2017) 834–848.

[24] V. Badrinarayanan, A. Kendall, R. Cipolla, Segnet: A deep convolutional encoder-decoder architecture for image segmentation, IEEE Transactions on Pattern Analysis and Machine Intelligence 39 (12) (2017) 2481–2495.

[25] A. Veeramuthu, S. Meenakshi, K. Ashok Kumar, A neural network based deep learning approach for efficient segmentation of brain tumor medical image data, Journal of Intelligent & Fuzzy Systems (Preprint) (2019) 1–8.

[26] B. Kim, J. C. Ye, Mumford-Shah loss functional for image segmentation with deep learning, IEEE Transactions on Image Processing 29 (2019) 1856–1866.

[27] P. Hu, B. Shuai, J. Liu, G. Wang, Deep level sets for salient object detection, in: Proceedings of Conference on Computer Vision and Pattern Recognition, 2017, pp. 2300–2309.

[28] J. Duan, J. Schlemper, W. Bai, T. J. Dawes, G. Bello, G. Doumou, Deep nested level sets: Fully automated segmentation of cardiac MR images in patients with pulmonary hypertension, in: Proceedings of International Conference on Medical Image Computing and Computer-Assisted Intervention, Springer, 2018, pp. 595–603.

[29] T. A. Ngo, Z. Lu, G. Carneiro, Combining deep learning and level set for the automated segmentation of the left ventricle of the heart from cardiac cine magnetic resonance, Medical Image Analysis 35 (2017) 159–171.

[30] A. Chambolle, P.-L. Lions, Image recovery via total variation minimization and related problems, Numerische Mathematik 76 (2) (1997) 167–188.

[31] T. M. Le, L. A. Vese, Additive and mutiplicative piecewise-smooth segmentation models in a functional minimization approach, Contemporary Mathematics 445 (2007) 207–224.

[32] K. Papafitsoros, C.-B. Schönlieb, A combined first and second order variational approach for image reconstruction, Journal of Mathematical Imaging and Vision 48 (2) (2014) 308–338.

[33] K. Papafitsoros, C. B. Schoenlieb, B. Sengul, Combined first and second order total variation inpainting using split Bregman, Image Processing On Line 3 (2013) 112–136.

[34] S. Wang, T.-Z. Huang, X.-L. Zhao, J.-J. Mei, J. Huang, Speckle noise removal in ultrasound images by first-and second-order total variation, Numerical Algorithms 78 (2) (2018) 513–533.

[35] W. Zhu, X. C. Tai, T. Chan, Image segmentation using Euler's elastica as the regularization, Journal of Scientific Computing 57 (2) (2013) 414–438.

[36] Q. Ma, J. Peng, D. Kong, Image segmentation via mean curvature regularized Mumford-Shah model and thresholding, Neural Processing Letters 48 (2) (2018) 1227–1241.

[37] L. Vese, A study in the BV space of a denoising-deblurring variational problem, Applied Mathematics and Optimization 44 (2) (2001) 131–161.

[38] J. Liang, X. Zhang, Retinex by higher order total variation L^1 decomposition, Journal of Mathematical Imaging and Vision 52 (3) (2015) 345–355.

[39] J. Duan, Z. Qiu, W. Lu, G. Wang, Z. Pan, L. Bai, An edge-weighted second order variational model for image decomposition, Digital Signal Processing 49 (2016) 162–181.

[40] M. Fukushima, Application of the alternating direction method of multipliers to separable convex programming problems, Computational Optimization and Applications 1 (1) (1992) 93–111.

[41] R. H. Chan, M. Tao, X. Yuan, Constrained total variation deblurring models and fast algorithms based on alternating direction method of multipliers, SIAM Journal on Imaging Sciences 6 (1) (2013) 680–697.

[42] S. Boyd, N. Parikh, E. Chu, B. Peleato, J. Eckstein, Distributed optimization and statistical learning via the alternating direction method of multipliers, Foundations and Trends® in Machine Learning 3 (1) (2011) 1–122.

[43] W. Deng, W. Yin, On the global and linear convergence of the generalized alternating direction method of multipliers, Journal of Scientific Computing 66 (3) (2016) 889–916.

[44] S. Yan, J. Liu, H. Huang, X.-C. Tai, A dual EM algorithm for TV regularized Gaussian mixture model in image segmentation, Inverse Problems & Imaging 13 (3) (2019) 653–677.

[45] T. Kanungo, D. M. Mount, N. S. Netanyahu, C. D. Piatko, R. Silverman, A. Y. Wu, An efficient k-means clustering algorithm: Analysis and implementation, IEEE Transactions on Pattern Analysis & Machine Intelligence (7) (2002) 881–892.

[46] C. Feng, W. Li, J. Hu, K. Yu, D. Zhao, BCEFCM_S: Bias correction embedded fuzzy c-means with spatial constraint to segment multiple spectral images with intensity inhomogeneities and noises, Signal Processing 168 (2020) 107347.

[47] J. C. De los Reyes, C.-B. Schönlieb, T. Valkonen, Bilevel parameter learning for higher-order total variation regularisation models, Journal of Mathematical Imaging and Vision 57 (1) (2017) 1–25.

[48] J. Spencer, K. Chen, J. Duan, Parameter-free selective segmentation with convex variational methods, IEEE Transactions on Image Processing 28 (5) (2018) 2163–2172.